Global and Planetary Change 229 (2023) 104221

Contents lists available at ScienceDirect

Global and Planetary Change

journal homepage: www.elsevier.com/locate/gloplacha

Marine Isotope Stage 4 (71–57 ka) on the Western European margin: Insights to the drainage and dynamics of the Western European Ice Sheet

Samuel Toucanne [a,*], Teresa Rodrigues [b,c], Guillemette Menot [d], Guillaume Soulet [a], Sandrine Cheron [a], Isabelle Billy [e], Frederique Eynaud [e], Pierre Antoine [f], Jaap S. Sinninghe Damste [g,h], Edouard Bard [i], Maria-Fernanda Sanchez Goñi [e,j]

[a] University of Brest, CNRS, Ifremer, Geo-Ocean, F-29280 Plouzane, France
[b] Portuguese Institute for Sea and Atmosphere (IPMA), 1495-165 Algès, Lisboa, Portugal
[c] Center of Marine Sciences (CCMAR), Algarve University, 8005-139 Faro, Portugal
[d] University of Lyon, ENS de Lyon, Univ Lyon 1, CNRS, UMR 5276 LGL-TPE, F-69364 Lyon, France
[e] University of Bordeaux, CNRS, Bordeaux INP, EPOC, UMR 5805, F-33600 Pessac, France
[f] University of Paris 1 UPEC, LGP, UMR-8591, Meudon, France
[g] NIOZ Royal Netherlands Institute for Sea Research, Department of Marine Microbiology and Biogeochemistry, 1790 AB Denbrurg, Texel, the Netherlands
[h] Department of Earth Sciences, Faculty of Geosciences, Utrecht University, Utrecht, the Netherlands
[i] CEREGE, Aix-Marseille University, CNRS, IRD, INRAE, Collège de France, Aix-en-Provence, France
[j] Ecole Pratique des Hautes Etudes (EPHE), PSL University, Pessac, France

ARTICLE INFO

Editor: Dr. Fabienne Marret-Davies

Keywords:
European Ice Sheet
Marine Isotope Stage 4
Climate dynamics
Northeast Atlantic
Bay of Biscay
Heinrich stadials
Quaternary
Deep-sea cores

ABSTRACT

Marine Isotope Stage (MIS) 4 (*ca.* 71–57 ka; within the Middle Weichselian Substage) is considered a significant Pleistocene glaciation, but it remains poorly constrained in comparison to that of the Late Weichselian Last Glacial Maximum (LGM; *ca.* 29–19 ka, during MIS 2), or even the Late Saalian MIS 6 (*ca.* 190–130 ka). Most MIS 4 glacial landforms in Europe were erased by the more extensive LGM ice advance, precluding a robust reconstruction of its extent and dynamic through time. Marine sedimentary archives, in preserving the source-to-sink sediment transfer signals of ice-sheet and glacier processes, help to bridge this gap. Here, the signals west of the European Ice Sheet (EIS) are tracked for MIS 4 from the deep Bay of Biscay (NE Atlantic), which was the outlet for Fennoscandian Ice Sheet (FIS) sediment-laden meltwater during extensive glaciations, specifically when the British-Irish Ice Sheet (BIIS) and the FIS coalesced into the North Sea (as during MIS 6 and the LGM). Sedimentological, geochemical, and mineralogical proxies reveal the absence of FIS-derived material in Bay of Biscay sediment throughout MIS 4, which indicates that FIS meltwater and huge river systems from the North European Plain never drained into the Bay of Biscay at that time. This suggests that contrary to MIS 6 and the LGM, the BIIS and FIS were not likely large enough to coalesce and form a (grounded) ice bridge onto the North Sea, thus confirming geomorphic evidence for a significant, but relatively limited, glaciation in Europe during MIS 4.

Closer to the Bay of Biscay, ice-marginal fluctuations of the BIIS are identified in the Celtic-Irish Sea region from the deep-sea record. More specifically, our findings suggest an early retreat of the Irish Sea Ice Stream as soon as *ca.* 68–65 ka, a few millennia before the demise of the EIS, and the Northern Hemisphere ice sheets as a whole, during Heinrich Stadial (HS) 6. This pattern is similar to that already recorded during MIS 2. Finally, this study reveals that the MIS 4 period in Western Europe corresponds, as for MIS 2, to a complex combination of general ice advance interspersed by preliminary-to-final EIS demises highlighted by HS conditions.

1. Introduction

Precise reconstructions of the timing and extent of past ice-sheet and glacier fluctuations are prerequisite for a thorough understanding of Earth's climate system. Such reconstructions exist for the North American Laurentide (LIS) and European ice sheets (EIS) but are limited to the Late Wisconsinan/Weichselian substages (in North America and Europe, respectively) during which these ice sheets reached their maximum

* Corresponding author.
E-mail address: Samuel.Toucanne@ifremer.fr (S. Toucanne).

https://doi.org/10.1016/j.gloplacha.2023.104221
Received 24 May 2023; Received in revised form 4 August 2023; Accepted 30 August 2023
Available online 1 September 2023

volume *ca.* 29–19 ka (corresponding to the Last Glacial Maximum -LGM-*sensu* Hughes et al., 2022b), and to the last deglaciation *ca.* 19–11 ka (Clark et al., 2009; Dalton et al., 2020; Hughes et al., 2016a; Palacios et al., 2020; Stroeven et al., 2016). Difficulties in dating terrestrial evidence of older glaciations has restricted pre-LGM reconstruction. However, to bridge this gap, terrestrial cosmogenic nuclide dating is evolving and increasingly applied (Allard et al., 2021; Balco, 2020) together with numerical modelling (Kleman et al., 2013; Seguinot et al., 2018) and reconstructions from deep-sea sediments (Colville et al., 2011; Wilson et al., 2018). These approaches reveal that the maximum extent of continental ice sheets and mountain glaciers are diachronous (*e.g.* Hughes et al., 2016a) and confirm, by extension, that changes in the global ice volume and sea level (as reconstructed using $\delta^{18}O$ of seawater) do not necessarily correspond to regional changes in ice extent (Gillespie and Molnar, 1995). For example, contrary to general expectation, Doughty et al. (2021) showed that the extent of many mountain glacier systems and some portions of the continental ice sheets was larger during Marine Isotope Stage (MIS) 4 (*ca.* 71–57 ka), when sea level was 80–100 m lower than at present (Cutler et al., 2003; Waelbroeck et al., 2002a) than during the LGM (during MIS 2), when sea level reached −110-130 m. Recent reconstructions of the Northern Hemisphere ice sheets demonstrate a significant build-up of ice to almost LGM extent at *ca.* 60 ka (Batchelor et al., 2019; Dalton et al., 2022). This likely indicates that MIS 4 can be regarded as a major Pleistocene glaciation (*e.g.* Ehlers and Gibbard, 2007). However, the MIS 4 glaciation is poorly constrained in comparison to the LGM and evidence for millennial-scale ice-sheet fluctuations at that time remain insufficient, especially for Europe (Rodríguez-Rodríguez et al., 2016; Salonen et al., 2008).

The volume of the EIS complex, extending from 11°west to 90°east, and composed of the British-Irish (BIIS; ~50–60°N), Fennoscandian (FIS; ~55–70°N) and Barents Sea ice sheets (BSIS; ~55–82°N), is estimated at 7–8 million km^3 (*ca.* 17–25 m sea level equivalent) during MIS 4 (Gowan et al., 2021; Patton et al., 2022; Fig. 1). This volume is roughly similar to that reported for the LGM (Hughes et al., 2016a) but the EIS

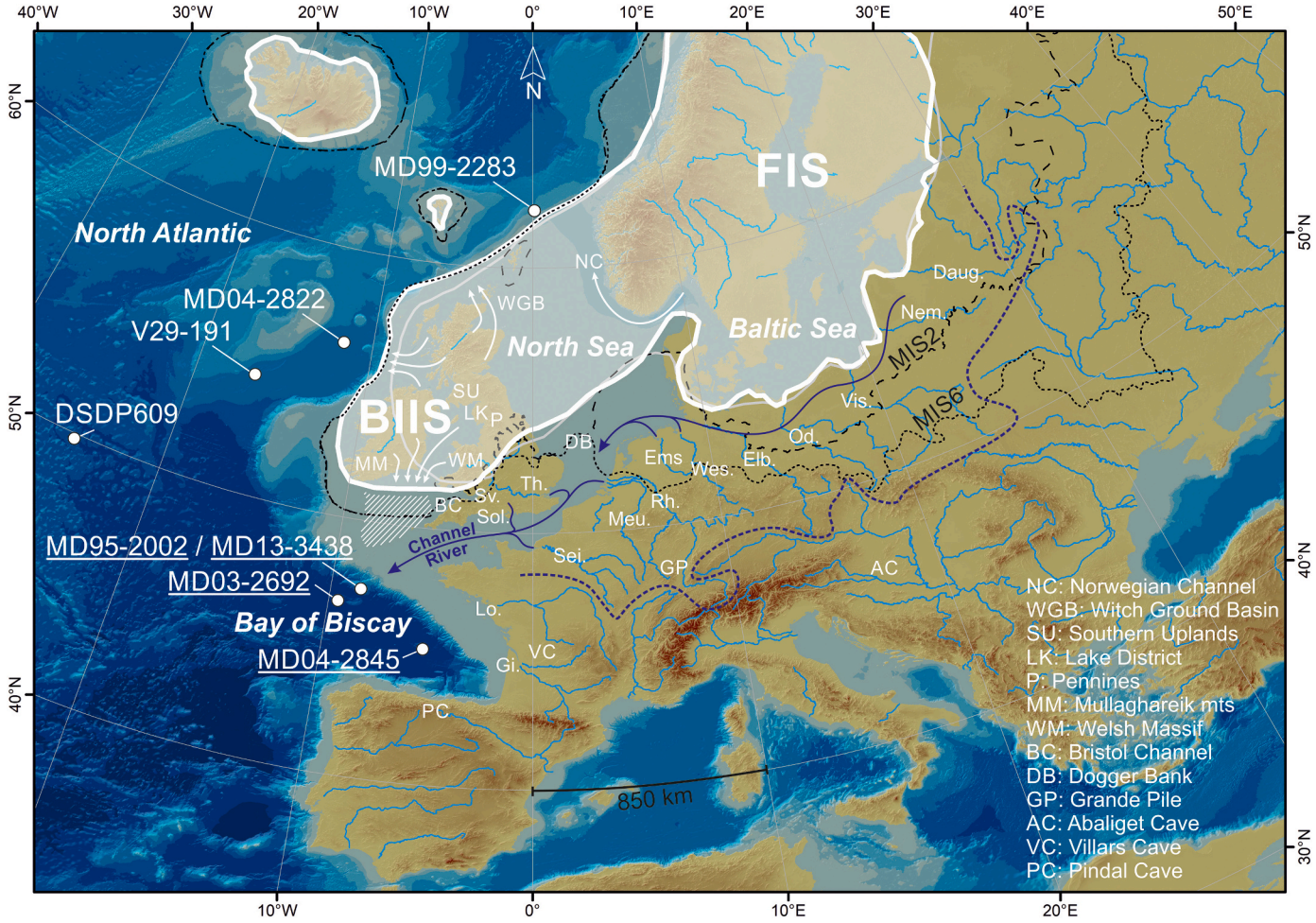

Fig. 1. Palaeogeography of Western Europe showing the glacial limits of the European Ice Sheet (EIS) complex, including the British-Irish (BIIS) and Fennoscandian (FIS) ice sheets, during MIS 4 (*ca.* 71–57 ka) according to Batchelor et al. (2019; thick white line) and Gowan et al. (2021; thin grey line). The glacial limits for MIS 2 (dashed black line) and MIS 6 (dotted black line) are shown for comparison (Batchelor et al., 2019). The coalescence of the BIIS and FIS in the North Sea proposed by Batchelor et al. (2019) and Gowan et al. (2021) for MIS 4 implies a routing of the central European rivers (*e.g.* Vistula, Oder, Elbe, Rhine, *etc.*), through ice-marginal meltwater spillways, towards the Channel River system (blue arrows; Gibbard, 1988), as shown for MIS 2 and MIS 6 (see the main text for details). Key sites discussed in the main text are identified here (*e.g.* the Witch Ground Basin -WGB- in the northern North Sea). The white shaded area on the Celtic Shelf depicts the extension of the Irish Sea Ice Stream (ISIS) *ca.* 27–26 ka (Clark et al., 2022). The southern limit of the Channel River catchment at its maximum extent (*e.g.* MIS 2, MIS 6; thick dashed black line), and the main European river systems (Gi.: Gironde, Lo.: Loire, Sv.: Severn, Sol.: Solent, Th.: Thames, Sei.: Seine, Meu.: Meuse, Rh.: Rhine, Ems, Wes.: Wesser, Elb.: Elbe, Od.: Oder, Vis.: Vistula, Nem.: Nemen, Daug.: Daugava), are also shown. The white arrows depict the main ice streams of the Western EIS. Core locations for DSDP609/V29–191, MD04–2822 (NE Atlantic) and MD99–2283 (northern North Sea margin) from McManus et al. (1994), Hibbert et al. (2010) and Lekens et al. (2009), respectively. Core locations for MD04–2845, MD03–2692 and MD95–2002/MD13–3438 in the Bay of Biscay from Sánchez Goñi et al. (2008), Mojtahid et al. (2005) and Grousset et al. (2000), respectively. (For interpretation of the references to colour in this figure legend, the reader is referred to the web version of this article.)

configuration differs between the two periods: the first, known as the Middle Weichselian glaciation (MIS 4), is far more extensive in the Kara Sea and Siberian sector, while the Late Weichselian glaciation (MIS 2) reached Northern Central Europe which was ice free since the second part of the Late Saalian MIS 6 *ca.* 150–130 ka (*e.g.* Svendsen et al., 2004). In the west, over Britain and Ireland, the LGM ice advance removed previous glacial landforms in most areas but sedimentary evidence (*e.g.* Courtmacsherry Raised Beach and overlying shallow marine sands in southern Ireland; Ó Cofaigh et al., 2012), together with exposure ages from ice-moulded bedrock in North Wales and in the Celtic Sea (Lundy Island), indicate the presence of ice over the Southern British Isles and the Celtic-Irish Sea during MIS 4 (Gibbard et al., 2017; Hughes et al., 2022a; Rolfe et al., 2012). Between the British Isles and Scandinavia, MIS 4 grounded ice is reported from geophysical and sedimentological data in the Witch Ground basin area (offshore NE Scotland, 58°N) of the central North Sea (Carr et al., 2006; Graham et al., 2011) and in the Norwegian Channel (Karmøy Stadial; Mangerud, 2004; Sejrup et al., 2000) (Fig. 1). Based on this evidence, it is thought that the BIIS and FIS coalesced in the North Sea during MIS 4 (*e.g.* Carr et al., 2006), consistent with the final stage of the last glacial cycle *ca.* 30 to 18 ka (Carr et al., 2000; Graham et al., 2007; Sejrup et al., 1994, 2009; Toucanne et al., 2010). This latter configuration led to the formation of a mega-river system (2.5×10^6 km^2; Patton et al., 2017), the so-called Fleuve Manche, or Channel River, that drained western Europe and the southern EIS as far east as northern central Europe, and finally flowed into the NE Atlantic (Bay of Biscay), the only possible outlet for meltwaters at that time (Gibbard, 1988; Grosswald, 1980). This drainage pattern is highly dependent on the regional ice extent and the associated isostatic adjustment (Busschers et al., 2007; Gibbard, 1995; Patton et al., 2017). However, previous studies highlight that Middle to Late Pleistocene EIS fluctuations, and specifically the melting episodes of the North Sea and Baltic ice streams, are recorded off the Channel River outlet, in the deep Bay of Biscay (46–48°N), for as long as the North Sea was covered by ice (Boswell et al., 2019; Toucanne et al., 2015). This routing is accurately highlighted during the early deglaciation *ca.* 20–17 ka when the rapid retreat of the western EIS (*ca.* 20–18 ka), leading to the unzipping of the BIIS and FIS and the subsequent ice-free conditions in the North Sea (*ca.* 17 ka; Hughes et al., 2016a), caused a dramatic increase followed by a cessation of FIS-derived sediment inputs into the Bay of Biscay (Ménot et al., 2006; Toucanne et al., 2010, 2015; Zaragosi et al., 2001). Recent geomorphic, seismic and stratigraphic evidence from the central and southern North Sea support this palaeoenvironmental evolution (Cotterill et al., 2017; Evans et al., 2021; Sejrup et al., 2016). No evidence for MIS 4 glaciation has been found so far in the southern North Sea (Gibbard et al., 2022; Laban and van der Meer, 2011), which is in agreement with the deposit of only thin loess sequences in northwest Europe (Antoine et al., 2016; Rousseau et al., 1998). However, recent EIS reconstructions for MIS 4 include, as for the LGM, a complete ice coverage of the central North Sea as far as 54–56°N south (Batchelor et al., 2019; Gowan et al., 2021; Greenwood et al., 2022; Fig. 1). Here earlier works on the deep Bay of Biscay are further developed to investigate MIS 4 sediment funnelled by the southern British Isles and Channel River. The configuration and dynamics of the EIS in the Celtic-Irish Sea and the North Sea region, and whether the central North Sea was indeed covered by ice, are also explored.

2. Materials and methods

This study is based on four Calypso long-piston cores from the Bay of Biscay, NE Atlantic (Fig. 1). The first set is located directly off the mouth of the Channel River, northern Bay of Biscay, with the twin cores MD95–2002 and MD13–3438 (Meriadzek Terrace; Labeyrie et al., 1995; Woerther, 2013) and core MD03–2692 (Trevelyan Escarpment; Bourillet and Turon, 2003). Previous studies have shown that these cores are suitable for reconstructing the deglacial pulses of meltwater emanating from the Western EIS (Eynaud et al., 2007; Fersi et al., 2021; Ménot et al., 2006; Mojtahid et al., 2005; Penaud et al., 2009; Toucanne et al., 2015; Zaragosi et al., 2001). These cores were compared with core MD04–2845 (Gascogne Seamount; Turon and Bourillet, 2004), located far from the Channel River influence, and in which terrestrial and marine proxies [pollen, foraminiferal oxygen isotopes, foraminifer-derived sea-surface temperatures (SSTs), iceberg-rafted debris (IRD)], provide a high-resolution palaeoenvironmental characterisation of Western Europe for the last climatic cycle (Sánchez Goñi et al., 2008, 2013). Details on cores and coring sites are given in Fig. 1 and Table 1.

To reconstruct EIS ice-margin fluctuations during MIS 4, the terrigenous and organic fluvial inputs in the northern Bay of Biscay were tracked through the quantification of terrigenous sediment fluxes and the use of appropriate molecular biomarkers, respectively. The geographical provenance of the sediment was explored by measuring the radiogenic neodymium (Nd) isotope ratios.

2.1. Terrigenous mass accumulation rates

The terrigenous mass accumulation rates (*t*MAR, in g cm^2 kyr^{-1}) were calculated at the Meriadzek Terrace (MD13–3438) and the Trevelyan Escarpment (MD03–2692) according to the following formula:

$$t\mathrm{MAR} = \mathrm{LSR} \times \mathrm{DBD} \times (1 - \text{carbonate content}) \quad (1)$$

where

LSR: Linear Sedimentation Rate (cm kyr^{-1}) and, DBD: Dry Bulk Density (g cm^{-3}), calculated assuming a mean grain density of 2.65 g cm^{-3} and an interstitial water density of 1.024 g cm^{-3} as follows:

$$\mathrm{DBD} = 2.65 \times (1.024 \times D\mathit{wet})/(1.024\text{–}2.65) \quad (2)$$

Wet bulk densities (D*wet*) were derived from gamma-ray attenuation density measurements. Details on coring disturbances and depth corrections (for the LSR calculation), carbonate content and physical properties measurements (including D*wet*) are described in Toucanne et al. (2009). Note that *t*MAR at the Meriadzek Terrace are from core MD13–3438 that benefit, contrary to the twin core MD95–2002 (Auffret et al., 2002; Toucanne et al., 2009), of high coring performance (as supported by the absence of sediment stretching and deformation) with the upgraded R/V Marion Dufresne CALYPSO corer (Bourillet et al., 2007; Govin et al., 2016).

2.2. Clay mineralogy

The clay mineralogy composition of MIS 4 sediments in core MD13–3438 ($n = 73$) was determined by X-ray diffractometry (XRD), using a D2 PHASER BRUKER model, a Bragg-Brentano device type equipped with a Cu X-ray tube, and the LYNXEYE Detector with a nickel filter (Ni 2.5). To separate the clays from the rest of the matrix, the sample underwent several stages of preparation: various chemical treatments to eliminate carbonates, iron oxides as well as the organic matter and a settling. Finally, these clays were plated on an oriented glass slide which was analysed in three different ways: without treatment, after saturation with ethylene glycol and after calcination at 490 °C (Moore and Reynolds, 1989). Measurements were made from 2 to 30° with a resolution of 0.02° lasting 1 s. The voltage and amperage were set to 30 kV and 10 mA, respectively. Peak areas of basal reflections for the main clay mineral groups (smectite-17 Å, illite-10 Å, and kaolinite/chlorite-7 Å), used to calculate the relative abundance of

Table 1
Core locations.

Core label	Lat. N	Long. W	Depth (m)	Cruise (year)
MD13–3438	47°27,13	8°27,03	2180	VT133-MERIADZEC (2013)
MD95–2002	47°27,12	8°32,03	2174	IMAGE1-MD101 (1995)
MD03–2692	46°49,72	9°30,97	4064	MD133-SEDICAR (2003)
MD04–2845	45°20,86	5°13,17	4175	MD142-ALIENOR 2 (2004)

clays, were estimated based on diffractograms of ethylene-glycolated samples using MacDiff software. The illite crystallinity (ICr, °Δ2Φ) index, or Kübler index (Kisch, 1991), was measured from the saturated ethylene glycol glass slide and represents the full width at half maximum (FWHM) determined from the illite peak at 10 Å (Chamley, 1989).

2.3. Analysis of biomarkers

Glycerol dialkyl glycerol tetraether (GDGT) lipids are membrane lipids, which are synthesised by archaea and bacteria (Schouten et al., 2013). Due to their contrasting relative abundances in the marine and continental realms, the branched and isoprenoid tetraether (BIT) index was initially proposed to reconstruct the input of terrestrial organic matter fluvially transported to the ocean (Hopmans et al., 2004): while bacteria thriving in soils and peats produce branched GDGTs (Weijers et al., 2006), crenarchaeol, a structurally related isoprenoid GDGT is characteristic of ubiquitous planktonic marine thaumarchaeta (Schouten et al., 2008; Sinninghe Damsté et al., 2002). Values of the BIT index are generally >0.9 in soils, but close to 0 in remote marine sediments (Weijers et al., 2006, 2014). Consequently, the BIT index has been increasingly used to trace the input of soil organic matter in different environments (*e.g.* Herfort et al., 2006; Ménot et al., 2006; Wu et al., 2013). However, subsequent work has revealed some complications in its application, *e.g. in-situ* production of branched GDGTs in marine sediments (Sinninghe Damsté, 2016) and aquatic production of crenarchaeol in river waters (De Jonge et al., 2014; Zell et al., 2013). However, in the vicinity of large river systems, marine BIT records can still be faithfully applied to reconstruct the input of fluvially transported organic matter (*e.g.* Zell et al., 2015). Since the BIT index is based on the abundance of brGDGTs, relative to that of crenarchaeol, which is linked to marine productivity, its use provides a first-order estimation of fluviatile organic matter input to a marine realm and should be cautiously applied in the continental realm (Schouten et al., 2013; Xiao et al., 2016).

After freeze-drying and grinding, 1 to 5 g aliquots of sediment horizons from the MD95–2002 core (n = 35) were extracted for GDGT analysis by the accelerated solvent extraction method (ASE 200 system, Dionex, California, USA) at 120 °C and 100 bars with dichloromethane/methanol (9:1, *v*/v) at CEREGE (France). The total lipid extract was subsequently separated into polar and apolar fractions using a column packed with Al_2O_3 using hexane/dichloromethane (9:1, v/v) and dichloromethane/methanol (1:1, v/v) as eluents, respectively at NIOZ (The Netherlands). The polar fraction was then filtered through a 0.45-μm, 4-mm diameter PTFE filter prior to injection. Following an initial set of analyses at NIOZ, GDGTs were then re-analysed at CEREGE by high-performance liquid chromatography/atmospheric pressure chemical ionisation mass spectrometry using a HP LC 1100 Series-MS (Hopmans et al., 2004; Sanchi et al., 2013). It should be noted that this method is not capable of separating the 5- and 6-methyl brGDGTs isomers as with the now commonly used method of Hopmans et al. (2016). However, to determine the BIT index, it is not necessary to separate the isomers and differences between the two methods are minor (Hopmans et al., 2016). In fact, application of the initial method for GDGT analysis (Hopmans et al., 2004) facilitates comparison of the record of the BIT index ratio obtained here with that previously reported for core MD95–2002 (Ménot et al., 2006).

Leaf wax *n*-alkanes are one of the lipid components in marine sediments, providing important insights into organic matter sources (Peters et al., 2005; Rodrigues et al., 2009). Here, long-chain (C_{23} to C_{33}) *n*-alkanes, wax lipids, synthesised by terrestrial higher plants to protect the plant cuticle (Eglinton and Hamilton, 1967) are used. The sedimentary *n*-alkane content results from net wax production and transport (*via* fluvial and aeolian) processes, where higher concentration in the sediments would result from either increased leaf wax production or higher leaf wax transport (Grimalt and Albaiges, 1990).

To quantify *n*-alkanes in sediment horizons (n = 54) in marine core MD13–3438, 2.5 g of sediments were freeze-dried, and homogenised. Before extraction, 10 μL of internal standard solution (*n*-hexatriacontane, tetracontane, and nonadecanol-1-ol) was added to the sediment samples. Biomarker lipids were extracted using dichloromethane in an ultrasonic bath (x3) and the combined extracts were subsequently hydrolysed with 6% potassium hydroxide in methanol. After derivatisation with bis (trimethylsilyl) trifluoroacetamide, the biomarker lipid extractions were analysed with a Varian gas chromatograph Model 3800 equipped with a septum programmable injector and a flame ionisation detector at IPMA (Portugal). The *n*-alkanes were identified by comparing the retention times to an external standard mixture (*n*-alkanes ranging from C_{17}-C_{36}). The *n*-alkanes concentration (ng/g, dry weight sample) was determined based on the internal standard *n*-hexatriacontane (C_{36}). In this study, it was considered that *n*-alkanes are likely predominantly derived from riverine particles and the Channel River, and not from aeolian transport (see Section 5.1 for details).

2.4. Radiogenic neodymium isotopes

Nd isotope ratios of fine-grained detrital fraction (<63 μm) from core MD13–3438 (n = 31) were analysed. The neodymium isotopic composition (εNd) of terrigenous sediment is a powerful tracer for geographical provenance because the εNd signature of detrital sediment is retained during continental weathering and subsequent transport (Bayon et al., 2015; Goldstein and Jacobsen, 1988). Here, the <63 μm fraction was targeted to track the precise origin of the river-sediment inputs from Western Europe (Boswell et al., 2019; Toucanne et al., 2015). Hence, this approach strongly differs from that of Grousset et al. (2000) which used the >150 μm fraction to examine the origin of IRD at the same site.

Dried fine-grained fractions (typically ~0.5 g) were crushed and digested by alkaline fusion (Bayon et al., 2009) after removal of all carbonate, Fe—Mn oxyde and organic components using a sequential leaching procedure (Bayon et al., 2002). Prior to analysis, the Nd fractions were isolated by ion chromatography (see details in Bayon et al., 2002). Isotopic measurements were performed at the Pôle Spectrométrie Océan, Brest (France), using a Thermo Scientific Neptune multi-collector ICPMS. Mass bias corrections on Nd were made with the exponential law, using $^{146}Nd/^{144}Nd = 0.7219$. Nd isotopic compositions were determined using sample-standard bracketing by analysing an in-house (SPEX-Nd) standard solution every two samples. Analyses of JNdi-1 standard solutions during the course of this study gave $^{143}Nd/^{144}Nd$ of 0.512113 ± 0.000005 (2 SD, n = 5), in agreement with the recommended value (0.512115) reported in Tanaka et al. (2000), and corresponding to an external reproducibility of ~ ± 0.11ε (2SD). Epsilon Nd values (εNd) were calculated using the chondritic (CHUR) $^{143}Nd/^{144}Nd$ value of 0.512638 (Jacobsen and Wasserburg, 1980).

2.5. X-ray fluorescence core scanner

The bulk intensity of major elements for late MIS 5 - early MIS 3 interval of cores MD95–2002/MD13–3438 and MD04–2845 was analysed using an Avaatech X-Ray Fluorescence (XRF) core scanner at the Institut Français de Recherche pour l'Exploitation de la Mer (IFREMER, France) and the University of Bordeaux (France), respectively. XRF data were measured every 10 mm along the entire length of the core, with a count time of 10 s, by setting the voltage to 10 kV (no filter) and the intensity to 600 mA. Only data for calcium (Ca; marine carbonate content) and iron (Fe; terrigenous-siliciclastic components) are reported in this study, through the use of the Ca/Fe ratio. The former is known to reflect climatically-driven biogenic carbonate fluxes and is considered, by extension, as a relevant proxy for regional-scale stratigraphic synchronisation (*e.g.* Hodell et al., 2015). Similar XRF data are available for the upper part of core MD95–2002 (Toucanne et al., 2015) as well as for cores MD13–3438 (Fersi et al., 2021) and MD03–2692 (Mojtahid et al.,

2005). They all show the footprint of the Heinrich Stadials (HS), *i.e.* stadials that contain a Heinrich event (HE) (Barker et al., 2009; Sánchez Goñi and Harrison, 2010), *i.e.* short-lived events of massive iceberg discharges (and hence IRD inputs) in the subpolar North Atlantic from the Hudson Strait Ice Stream (Hemming, 2004; Fig. 2).

3. Chronology

The revised chronology of cores MD13–3438 (Fersi et al., 2021), MD03–2692 (Eynaud et al., 2007) (as far back as *ca.* 85 ka) and MD04–2845 (for the *ca.* 85–44 ka interval; Sánchez Goñi et al., 2008) is based on the synchronisation of high-resolution XRF Ca/Fe ratios, reflecting climatically-driven biogenic carbonate fluxes (*e.g.* Hodell et al., 2013), with that of the reference core MD95–2002 (Fig. 2). MD95–2002 core chronology (here extended to *ca.* 85 ka) is based on 30 ^{14}C dates and 28 identified calendar tie-points (Tables 2 and 3) obtained through aligning polar planktonic *Neogloboquadrina pachyderma* (*s.s.* sinistral) abundances and XRF Ca/Fe ratios (*per* Toucanne et al., 2021) to the composite Asian Monsoon (AM; Hulu/Sanbao) δ^{18}O record (Cheng et al., 2016, 2018; Southon et al., 2012; Wang et al., 2001, 2008). Recent independent evidence of synchronous glacial high-latitude-to-tropical coupling of climate changes support this approach (Corrick et al., 2020). The ^{14}C dates were obtained from the ^{14}C measurement of monospecific planktonic foraminifer samples. These dates have been published with methods detailed in the original publications (*e.g.* Eynaud et al., 2007; Grousset et al., 2000; Toucanne et al., 2021). The ^{14}C dates were calibrated (Christen and Pérez, 2009) using the Marine20 calibration curve (Heaton et al., 2020). Before calibration the ^{14}C dates were corrected for a local marine reservoir age adjustment (ΔR) according to an approach recently developed and recommended by Heaton et al. (2023). The approach and the reasons why this approach should be used are extensively discussed elsewhere (Heaton et al., 2023). In brief, the oceanic carbon cycle now used to model the Marine20 calibration curve (Heaton et al., 2020) does incorporate global-scale surface ocean ^{14}C changes that occurred in the glacial period (Heaton et al., 2023). However, in polar regions (*e.g.* latitude higher than 40° in the Northern Hemisphere), an extra marine reservoir age correction is needed because significant additional localised changes in surface-water ^{14}C concentration occurred during the glacial period (Butzin et al., 2005) that are not captured by the global-scale Marine20 curve (Heaton et al., 2023). Thus, following Heaton et al. (2023) recommendations, the ^{14}C dates have been corrected for marine reservoir age (ΔR) as follows: i) the Holocene ΔR^{Hol} value was set to -155 ± 60 ^{14}C yrs., calculated based on 17 local pre-bomb ΔR values from locations within 500 km around the core location (Faivre et al., 2019; Harkness, 1983; Mangerud et al., 2006; Monge-Soares, 1993; Tisnérat-Laborde et al., 2010). These ΔR values are available in the maintained marine reservoir database at http://calib.org/marine/ (Reimer and Reimer, 2001). For the glacial period (pre-Holocene), an extra ΔR correction must be added to that of the Holocene ΔR^{Hol}. The extra value $\Delta R^{Hol->GS}$ is estimated to be 420 ^{14}C yrs. at latitude 46.25°N close to that of the core location (Heaton et al., 2023). Thus, the local maximum ΔR correction for the glacial is $\Delta R^{GS} = \Delta R^{Hol} + \Delta R^{Hol->GS} = 265$ ^{14}C yrs. However, the ΔR^{GS} value was parametrised as 55 ± 105 ^{14}C yrs. so that ΔR^{GS} covers the range $-$ 155 to 265 ^{14}C at 95%, *i.e.* the expected ΔR minimal and maximal values for the glacial period. Note that the local marine reservoir age ΔR is as defined in Stuiver et al. (1986) and Stuiver and Braziunas (1993). The identified tie-points are calendar ages and do not need to be calibrated. The whole set of dates was entered into the Bayesian age-depth modelling software Bacon (Blaauw and Christen, 2011). The model needs a set of parameters to be run. The thickness parameter was set to 30 cm (thick = 30), the uncertainty on the marine reservoir age was set to -155 ± 60 ^{14}C yrs. for Holocene ^{14}C dates and to 55 ± 105 ^{14}C yrs. for glacial ^{14}C dates (as discussed above). A boundary was set at depth 2300 cm and the prior value on the accumulation rate below the boundary was set to 100 yrs. cm^{-1} and above the boundary to 20 yrs. cm^{-1} (acc. Mean = c(20,100)). The sample size governing the number of Markov chain Monte Carlo (MCMC) iterations was set to 10,000 (ssize = 10,000). All other parameters were left at their default value.

4. Results

4.1. Terrigenous mass accumulation rates

The *t*MAR at the Meriadzek Terrace (MD13–3438) are <5–10 g cm^2 kyr^{-1} for late MIS 5, abruptly increase to 20 g cm^2 kyr^{-1} during early MIS 4 (GI-19.2, *ca.* 70 ka) and reach a plateau at around 30–40 g cm^2 kyr^{-1} during MIS 4 (Fig. 3). At the Trevelyan Escarpment (MD03–2692), the *t*MAR are significantly lower but show a similar pattern to the one identified on the Meriadzek Terrace. The *t*MAR are <5–10 g cm^2 kyr^{-1} for late MIS 5 and early MIS 4 then increase during MIS 4, to reach 10–30 g cm^2 kyr^{-1} (Fig. 4). At both sites, maximum MIS 4 *t*MAR at the two sites are coeval with HS 6, then decrease (to 10–20 g cm^2 kyr^{-1}) during early MIS 3 (GI-17, *ca.* 60–58 ka).

4.2. Clay mineralogy

Illite dominates over the studied interval (45–57%), and smectite, chlorite and kaolinite reach maximum values of 10–20% each (not shown). Illite crystallinity (ICr; $\Delta 2\Phi$) show values of 0.26–0.33 during late MIS 5 and early MIS 3, and a significant peak is observed during the first part of MIS 4 (*i.e.* during GS-19.1) with values up to 0.41 reached just before GI-18 (*ca.* 65 ka), when ICr values drop sharply down to 0.28. Kaolinite peaks to 20% during GS-19.1 then decreases to 13% during GI-18 (Fig. 3). No trends are observed in the other mineralogical data.

4.3. Biomarkers: BIT-index and n-alkanes

The BIT-index shows values ranging from 0.02 to 0.23 from late MIS 5 to early MIS 3 (Fig. 3). Maximum values are observed during MIS 4, with peak values of 0.23 and 0.13 during the GS-19.1 and HS 6, respectively. The *n*-alkanes show values ranging from 300 ng/g during late MIS5 to 1800 ng/g during MIS 4 and the GS-19.1. A decreasing trend is observed throughout MIS 4, with contents of 500–700 ng/g during early MIS 3. It is noticeable that both the BIT-index and *n*-alkanes show decreasing values at time of GI-18 (Fig. 3).

4.4. Radiogenic neodymium isotopes

The εNd record shows values ranging from −11 to −12.2, with a mean value of -11.4 ± 0.3 over MIS 4. The maximum values (−11 to −11.2) are found in the early part of GS-19.1, at the end of HS 6 and at the MIS 4–3 transition (*ca.* 60 ka). On the other hand, the minimum value of −12.2 is observed during the second part of the GS-19.1 interval. This εNd minima is embedded in five GS19.1 sediment characterised by εNd values lower than −11.8. A significant increase in εNd coeval with GI-18 (Fig. 3).

5. Discussion

5.1. The Channel River catchment during MIS 4: palaeoenvironmental implications

5.1.1. Regional drainage evolution and its impact on Bay of Biscay sedimentation

Sedimentation in the northern Bay of Biscay varied dramatically throughout the descent into the last ice age (late MIS 5) and during MIS 4, when the strong thermal gradient between cold air and the warmer NE Atlantic fed moisture over the British Isles and Scandinavia and favoured the rapid growth of the EIS (Sánchez Goñi et al., 2013). A 6–8 fold increase in terrigenous accumulation rates starts at site MD13–3438

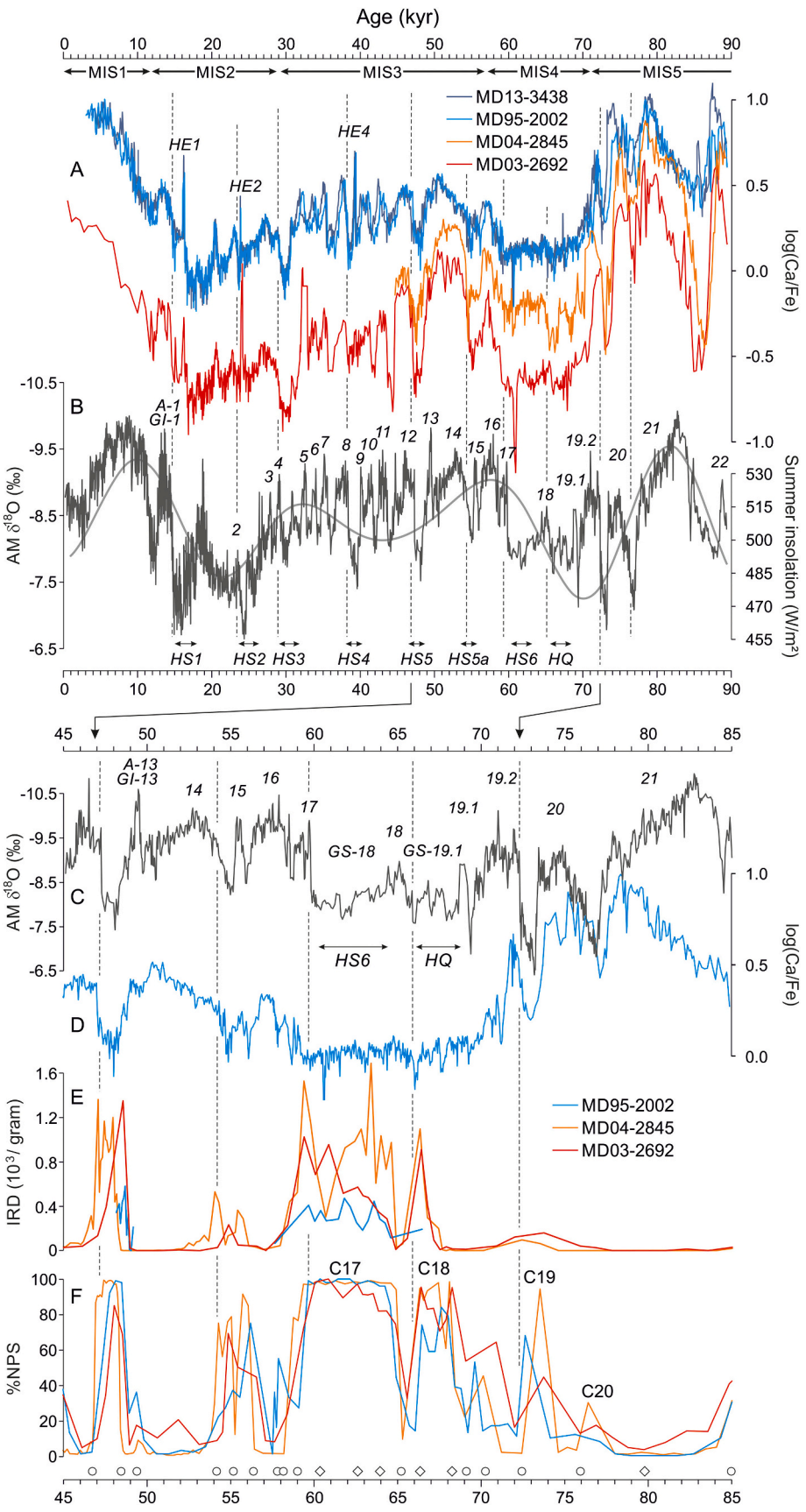

Fig. 2. (A, D) XRF log (Ca/Fe) (Fersi et al., 2021; Mojtahid et al., 2005; Toucanne et al., 2015); (B, C) the composite AM $\delta^{18}O$ record (Cheng et al., 2016); (E) normalised counts of iceberg-rafted detritus (IRD; Grousset et al., 2000; Mojtahid et al., 2005; Sánchez Goñi et al., 2008); (F) relative abundances of the polar planktonic foraminifera *N. pachyderma* s. (% NPS; Grousset et al., 2000; Mojtahid et al., 2005; Sánchez Goñi et al., 2008). The summer (June) insolation at 45°N (B) is also shown (Laskar et al., 2004). Open circles in the lower part of the figure depict the chronological control points obtained through aligning both *N. pachyderma* s. abundances and/or XRF log (Ca/Fe) ratios to the composite AM $\delta^{18}O$ record (see Table 2 for details). Open diamonds depict core-to-core (XRF-based) correlations (without AM counterpart) that improve the regional stratigraphic synchronisation. Stratigraphic events from the composite AM $\delta^{18}O$ record (Chinese Interstadials A1-A22; Cheng et al., 2006; Wang et al., 2008) and their equivalent in the Greenland ice-core records (GI-1 to GI-22; Rasmussen et al., 2014). Numbered marine polar episodes (C17 to C20) from sites DSDP609 and V29–191, NE Atlantic (Fig. 1; McManus et al., 1994). GS: Greenland stadials; HE: Heinrich events; HS: Heinrich stadials (including HQ, see Bassis et al., 2017 and Zhou et al., 2021).

Table 2
Chronological framework (tie-points) for cores MD13–3438, MD04–2845 and MD03–2692 (see their location of Fig. 1) based on their synchronisation (depth scale) to reference core MD95–2002 (age scale; see Table 3 and 'Chronology' section for details) *via* the XRF log (Ca/Fe) ratio (Fig. 2). Regional stratigraphic nomenclature (*e.g.* LGM-*n*, HS1-n, *etc.*) according to Toucanne et al. (2021). Core-to-core (XRF-based) correlations without Hulu counterpart (*ca.* 68–60 ka) are used to improve the regional stratigraphic synchronisation. Stratigraphic events from Hulu Cave (Hulu Chinese Interstadials A1-A22; Cheng et al., 2006; Wang et al., 2008) and their equivalent in the Greenland ice-core records (GI-1 to GI-22; Rasmussen et al., 2014). LGM- (1 to 9) refers to the Last Glacial Maximum. HS (HS1 to 4) refers to Heinrich stadials. HE (1 to 4) refers to Heinrich events (*i.e.* discharge of icebergs from the Hudson Strait Ice Stream of the LIS to the North Atlantic). GS: Greenland stadials; YD: Younger Dryas.

Stratigraphic label	MD95–2002	Age[a]	MD13–3438	MD04–2845	MD03–2692
	Depth (cm)	(cal kyr BP)	Depth (cm)	Depth (cm)	Depth (cm)
End YD	201	11.64	150	–	42
Start YD	262	12.71	187	–	75
HS1–7 (Start A1 / GI-1e)	385	14.69	254	–	106
HS1–6 (HE1 *s*)	455	16.19	292	–	132
HS1–5	515	16.63	328	–	161
HS1–4	548	16.79	338	–	183
HS1–3	690	17.27	441	–	212
HS1–2	745	17.46	488	–	264
HS1–1	865	17.86	579	–	296
LGM-9	940	18.31	630	–	352
LGM-8	970	18.51	651	–	374
LGM-7	1000	18.70	674	–	394
LGM-6	1040	18.96	708	–	438
LGM-5	1145	19.65	799	–	523
LGM-4	1230	20.24	868	–	583
LGM-3	1260	20.78	892	–	614
LGM-2 (End A2 / GI-2.1)	1340	22.47	963	–	714
LGM-1	1355	22.85	972	–	731
HS2–4 (Start A2 / GI-2.2)	1415	23.63	1022	–	770
HS2–3 (HE2 *ss*)	1460	23.83	1061	–	797
HS2–2	1495	24.52	1094	–	823
HS2–1 (End A3 / GI-3)	1550	26.27	1134	–	898
Start A3 / GI-3	1591	27.92	1187	–	944
HS3–4 (Start A4 / GI-4)	1635	29.05	1224	–	980
HS3–3	1695	29.90	1297	–	1010
HS3–2 (End GI-5.1)	1745	30.69	1349	–	1048
HS3–1 (End A5 / GI-5.2)	1779	31.81	1384	–	1070
Start A5 / GI-5.2	1793	32.63	1398	–	1100
Start A6 / GI-6	1825	34.06	1432	–	1150
Start A7 / GI-7c	1858	35.50	1467	–	1181
HS4–3 (Start A8 / GI-8c)	1906	38.24	1520	–	1200
HS4–2 (HE4 *ss*)	1966	39.34	1581	–	1242
HS4–1 (End A9 / GI-9)	1990	40.11	1607	–	1270
Start A9 / GI-9	2000	40.61	1617	–	1286
Start A10 / GI-10	2013	41.34	1632	–	1298
Start A11 / GI-11	2044	43.58	1669	–	1337
Start GS-12	2059	44.63	1683	1312	1350
Start A12 / GI-12c	2090	46.74	1722	1339	1364
Start GS-13	2129	48.48	1770	1386	1398
Start GS-13c	2150	49.40	1791	1401	1420
Start A14 / GI-14e	2218	54.16	1878	1453	1458
Start A15 / GS-15.2	2240	55.16	1903	1466	1488
Start GS-16.1	2262	56.356	1928	1484	1496
Start A16 / GI-16.2	2300	57.78	1971	1522	1522
Start GI-17.1c	2314	58.15	1986	1532	1528
Start A17 / GI-17.2	2328	58.99	2003	1521	1534
–	2359	60.36	2040	1554	1554
–	2422	62.62	2116	1593	1580
–	2460	63.95	2162	1638	1622
Mid A18 / GI-18	2497	65.22	2203	1679	1646
–	2527	66.36	2234	1690	1658
–	2576	68.29	2298	1777	1710
Mid GI-19.1	2597	69.10	2320	1791	1720
Start GS-19-2	2623	70.27	2348	1801	1724
Start A19 / GI-19-2	2666	72.46	2395	1810	1744
Start A20 / GI-20c	2692	75.95	2443	1842	1760
–	2729	79.77	2498	1866	1800
Start A21 / GI-21.2	2773	84.87	2567	1906	1840
Start A22 / GI-22 g	2801	89.36	2611	1938	1866

[a] Ages given by the age modelling software Bacon (Blaauw and Christen, 2011) and the chronological constraints summarized in Table 3.

around 70 ka, as soon as the end of the long-lasting GI-19.2, and rates remained high until the end of HS 6 at *ca.* 60 ka (Fig. 3). This change in terrigenous input is supported independently by the BIT-index and the concentration of terrestrial *n*-alkanes, which are biomarker proxies used to reconstruct the relative fluvial input of terrestrial organic matter in the marine environment (see Section 2.3), with values at around 70–60 ka that are noticeably higher than those at MIS 5 and early MIS 3 (Fig. 3). Due to their methodological distinctiveness and corresponding

Table 3
The radiocarbon ages and calendar tie-point (from Hulu Cave; *e.g.* Cheng et al., 2016) used to reconstruct the age-depth model of core MD95–2002. See 'Chronology' section for further information [Ref. 1: Zaragosi et al., 2001; 2: Zumaque et al., 2017; 3: Cheng et al., 2018, Cheng et al., 2016, Southon et al., 2012, Wang et al., 2001; 4: Zaragosi et al., 2006; 5: Toucanne et al., 2008; 6: Eynaud et al., 2007; 7: Toucanne et al., 2021; 8: Grousset et al., 2000; 9: Auffret et al., 2002]. Stratigraphic events from Hulu Cave (Hulu Chinese Interstadials A1-A22; Cheng et al., 2006; Wang et al., 2008) and their equivalent in the Greenland ice-core records (GI-1 to GI-22; Rasmussen et al., 2014). GS: Greenland stadials; YD/PB: Younger Dryas / Preboreal.

Core label	Depth (cm)	Depth in core MD95–2002 (cm)	Lab. number	Species	^{14}C age (yr BP)	Error (1σ)	Cal. age (yr BP)	Error (1σ)	Ref.
MD95–2002	0	0	LSCE-99360	*G. bull*	2060	70	–	–	1
MD95–2002	34	34	OS-98831	*G. bull*	4235	25	–	–	2
MD95–2002	72	72	OS-98831	*G. bull*	7145	35	–	–	2
MD95–2002	104	104	OS-98831	*G. bull*	8915	40	–	–	2
MD95–2002	140	140	LSCE-99361	*G. bull*	9480	90	–	–	1
YD/PB	–	195–205	–	–	–	–	11,610	40	3
MD95–2002	240	240	LSCE-99362	*N. pch(s)*	11,190	100	–	–	1
MD03–2690	626	371–379	SacA-003234	*G. bull*	13,020	60	–	–	4
A1 / GI-1e	–	380–390	–	–	–	–	14,674	50	3
MD03–2690	692	389–397	SacA-003235	*N. pch(s)*	13,170	70	–	–	4
MD95–2002	420	420	LSCE-99363	*N. pch(s)*	13,730	130	–	–	1
MD95–2002	454	454	LSCE-99364	*N. pch(s)*	14,200	110	–	–	1
MD95–2002	463	463	LSCE-99365	*N. pch(s)*	14,420	120	–	–	1
MD95–2002	510	510	LSCE-99366	*N. pch(s)*	14,570	130	–	–	1
MD95–2002	550	550	SacA-003242	*N. pch(s)*	14,830	70	–	–	4
MD95–2002	580	580	Beta-141,702	*N. pch(s)*	14,810	200	–	–	1
MD95–2002	869	869	SacA-003243	*N. pch(s)*	15,300	70	–	–	4
MD95–2002	875	875	SacA-003244	*N. pch(s)*	15,280	160	–	–	4
MD03–2690	2923	1210–1216	SacA-005972	*G. bull*	17,390	110	–	–	5
MD03–2692	580	1220–1225	SacA-001905	*G. bull*	17,290	90	–	–	6
MD95–2002	1320	1320	SacA-003245	*G. bull*	18,850	90	–	–	4
MD95–2002	1340	1340	SacA-003246	*G. bull*	19,430	100	–	–	4
MD95–2002	1370	1370	ETH-75010	*G. bull*	20,148	70	–	–	7
MD95–2002	1390	1390	SacA-003247	*G. bull*	20,620	80	–	–	4
A2 / GI-2.2	–	1415	–	–	–	–	23,744	70	3
MD95–2002	1424	1424	Beta-123,696	*N. pch(s)*	20,240	60	–	–	8
MD95–2002	1453	1453	Beta-123,698	*N. pch(s)*	20,430	80	–	–	8
MD95–2002	1464	1464	Beta-123,699	*N. pch(s)*	20,600	80	–	–	8
MD95–2002	1534	1534	Beta-123,697	*N. pch(s)*	22,250	70	–	–	8
A3 / GI-3	–	1590–1593	–	–	–	–	27,945	75	3
MD95–2002	1610	1610	Beta-99,367	*N. pch(s)*	24,410	250	–	–	9
A4 / GI-4	–	1635	–	–	–	–	29,117	75	3
MD95–2002	1664	1664	Beta-99,368	*N. pch(s)*	25,820	230	–	–	9
GI-5.1	–	1756	–	–	–	–	30,871	135	3
A5 / GI-5.2	–	1793	–	–	–	–	32,647	135	3
A6 / GI-6	–	1825	–	–	–	–	34,034	175	3
A7 / GI-7c	–	1858	–	–	–	–	35,501	110	3
A8 / GI-8c	–	1906	–	–	–	–	38,284	90	3
MD95–2002	1948	1948	GifA-100,123	*N. pch(s)*	34,320	520	–	–	9
MD95–2002	1976	1976	GifA-100,124	*N. pch(s)*	35,480	520	–	–	9
A9 / GI-9	–	2000	–	–	–	–	40,255	190	3
A10 / GI-10	–	2013	–	–	–	–	41,659	220	3
A11 / GI-11	–	2044	–	–	–	–	43,581	80	3
A12 / GI-12c	–	2096–2098	–	–	–	–	47,232	145	3
A13 / GI-13c	–	2155	–	–	–	–	49,610	130	3
A14 / GI-14e	–	2218	–	–	–		54,229	521	3
GS-15.2	–	2240	–	–	–		55,261	530	3
GS-16.1	–	2262	–	–	–		56,232	320	3
A16 / GI-16.2	–	2300	–	–	–		58,542	635	3
GI-17.1c	–	2314	–	–	–		59,337	855	3
A17 / GI-17.2	–	2328	–	–	–		59,770	730	3
A18 / GI-18 (mid)	–	2497	–	–	–		65,076	740	3
GI-19.1 (mid)	–	2597	–	–	–		68,844	985	3
GS19–2	–	2623	–	–	–		70,125	740	3
A19 / GI-19-2	–	2666	–	–	–		72,273	400	3
A20 / GI-20c	–	2692	–	–	–		76,227	640	3
A21 / GI-21.2	–	2773	–	–	–		84,277	950	3
A22 / GI-22 g	–	2801	–	–	–		89,749	675	3

environmental meaning (regarding sediment, soil, or vegetation; *e.g.* Eglinton and Hamilton, 1967; Schouten et al., 2013), these two proxies, as well as the terrigenous accumulation rates, reveal their own evolution and structures throughout MIS 4. They all, however, point to an increase in continental-derived material inputs into the northern Bay of Biscay during MIS 4. Eustatic sea-level changes are a primary forcing since the lowstand conditions of MIS 4 (−80–100 m; Cutler et al., 2003; Waelbroeck et al., 2002b) forced the westward migration of the modern, Western European rivers (*e.g.* Loire, Severn) across the emerged continental shelf, thus increasing terrigenous inputs on the Bay of Biscay slope. This is clearly illustrated by the abrupt 30–40 m sea-level fall that occurred in the early MIS 4, *ca.* 71–68 ka, and the concomitant abrupt increase in terrigenous inputs (*t*MAR) at site MD13–3438 (Fig. 4). This pattern is reinforced by an increase in on-land sediment availability, which is primarily caused by a reduction in vegetation cover (Dosseto et al., 2010), as evidenced in Western Europe by the gradual replacement of Atlantic and boreal forests by steppic environments (Sánchez Goñi et al., 2008, 2013; Fig. 3), and by the development of the Channel

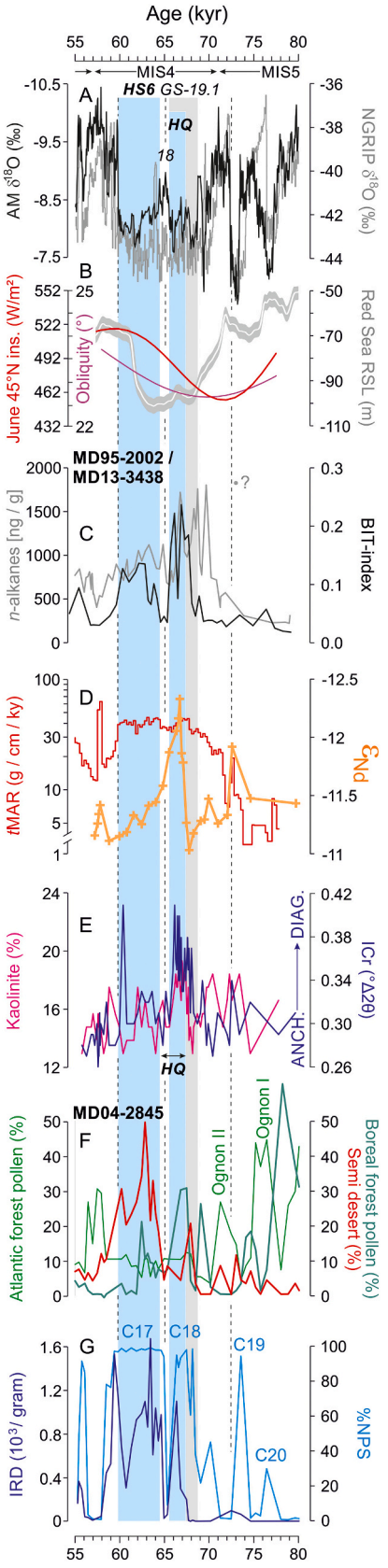

(caption on next column)

Fig. 3. (A) The composite AM $\delta^{18}O$ record (Cheng et al., 2016) and the NGRIP $\delta^{18}O$ record (GICC05 modelext timescale; Rasmussen et al., 2014; Seierstad et al., 2014); (B) June insolation at 45°N, obliquity (Laskar et al., 2004) and the Red Sea relative sea-level record (AM timescale; Grant et al., 2014); (C) summed concentration of C_{23}-C_{33} alkanes at site MD13–3438 (anomalous result at 74 ka is indicated by a question mark), and the record of the branched and isoprenoid tetraether (BIT) index at site MD95–2002; (D) terrigenous mass accumulation rates and the neodymium isotopic composition (expressed in εNd) at site MD13–3438; (E) kaolinite content and illite crystallinity (ICr) at site MD13–3438. ICr allows to distinguish between metamorphic (anchizone, ANCH.) *versus* non metamorphic (burial diagenesis, DIA.) illite sources (Kubler, 1967); (F) Pollen percentage changes of three vegetation types at site MD04–2845 (Sánchez Goñi et al., 2008, 2013). The highest percentages of the temperate Atlantic forest identify the Ognon I and II warm phases (interstadials) first recognised in La Grande Pile pollen sequence, NE France (Woillard, 1978); (G) normalised counts of iceberg-rafted detritus (IRD) and relative abundances of the polar planktonic foraminifera *N. pachyderma* s. (% NPS) at site MD04–2845 (Sánchez Goñi et al., 2008). Numbered marine polar episodes (C17 to C20) from sites DSDP609 and V29–191, NE Atlantic (Fig. 1; McManus et al., 1994). GS-: Greenland stadials; HS: Heinrich stadials (including HQ, see Bassis et al., 2017 and Zhou et al., 2021). (For interpretation of the references to colour in this figure legend, the reader is referred to the web version of this article.)

River, which significantly increases the catchment of the Bay of Biscay basin. This includes catchments of the northern French (*e.g.* Seine, Somme) and southern British rivers (*e.g.* Solent) (Antoine et al., 2003) and, during EIS glacial maxima, those of the Thames, Rhine and northern central European rivers (Elbe, Oder, Vistula, Daugava; Gibbard, 1988) (Fig. 1). This major drainage reorganisation can be tracked through inorganic sediment geochemistry and the Nd isotopic ratios. The westward routing of the northern central European rivers, combined with FIS sediment-laden meltwaters from the Baltic region (Fig. 1), causes the arrival of 'old' (Precambrian) unradiogenic sediment (Table 4) into the northern Bay of Biscay, with εNd values < -13 that significantly differ from those found today (-11 at core tops) and derived from 'younger' (Phanerozoic) Western European formations (*e.g.* Parra et al., 1998). Such transient, unradiogenic excursions (εNd down to -14.1) have been reported for MIS 2 and MIS 6 (Fig. 4), when melting FIS flushed the glacigenic sediment of northern central Europe ($-14.8 <$ εNd < -13.1; Table 4) and increased the Baltic contribution to the Channel River system (Boswell et al., 2019; Toucanne et al., 2015). Below, the possibility that northern central European rivers and the southern FIS drained into the Channel River during MIS 4 is explored.

5.1.2. Was the Channel River connected to the North European Plain and the southern EIS during MIS 4?

εNd values in MIS 4 sediment at site MD13–3438 range from -11 to -12.2. Late MIS 5 and early MIS 3 were distinguished by values greater than -11.5, similar to those found for the early MIS 5 and MIS 1 (Boswell et al., 2019). A minimum (*i.e.* unradiogenic) value of -12.2 is reported during GS-19.1 (*ca.* 66 ka). This interval is coeval with sea-level lowstand conditions (Fig. 3). Thus, the associated εNd signature most likely highlights the palaeogeographical shifts outlined above and the Channel River regional imprint. However, MIS 4 εNd values differ significantly from those reported for MIS 6 and MIS 2 (Fig. 4), implying a substantially distinct palaeogeography for the MIS 4 Channel River watershed. More specifically, the absence of Baltic-type εNd values (*i.e.* North European Plain clusters in Table 4) in the northern Bay of Biscay sediment suggests that the Channel River did not drain the North European Plain or the Baltic Shield during MIS 4. As a result, the Channel River watershed was undoubtedly limited to the northern French (Seine, Somme) and Belgian rivers (Schelde, possibly combined with the Rhine; Hijma et al., 2012) and the southern British Isles during MIS 4. This reduced configuration for the Channel River catchment, and the absence of FIS erosional imprint (*e.g.* Patton et al., 2022) in its upstream part, explain the low MIS 4 terrigenous flux and BIT-index values in the

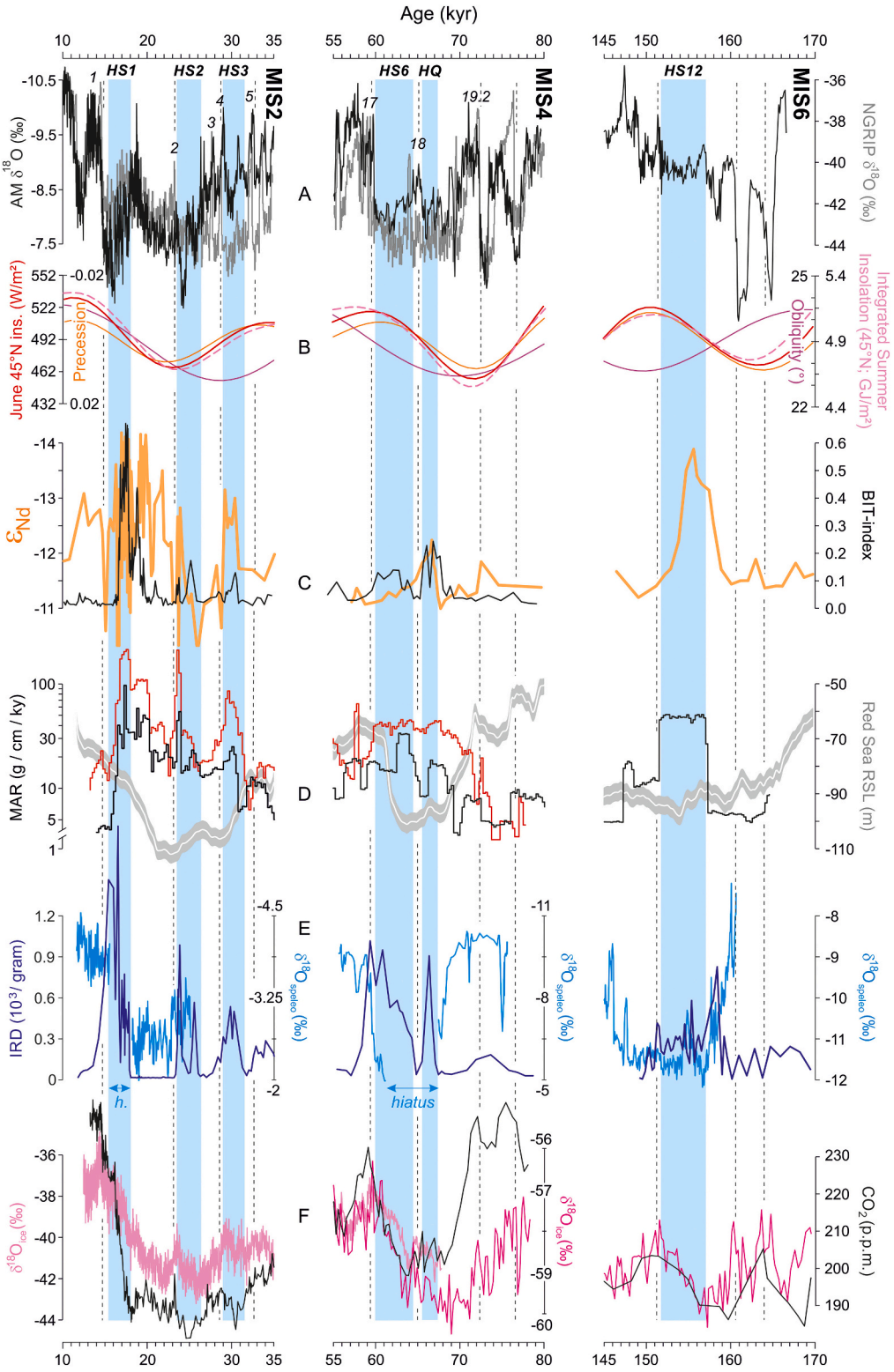

Fig. 4. (A) The composite AM $\delta^{18}O$ record (Cheng et al., 2016) and NGRIP $\delta^{18}O$ record (GICC05 modelext timescale; Rasmussen et al., 2014; Seierstad et al., 2014); (B) June insolation and integrated summer energy at 45°N ($\tau \sim 400$), and the precession and obliquity (Huybers, 2006; Laskar et al., 2004); (C) neodymium isotopic composition (expressed in εNd) and BIT-index at the Meriadzek Terrace (sites MD95–2002 and MD13–3438) for MIS 2 (Ménot et al., 2006; Toucanne et al., 2015) and MIS 4 (this study). MIS 6 εNd data from Boswell et al. (2019); (D) terrigenous mass accumulation rates at sites MD13–3438 (red lines; this study) and MD03–2692 (black lines; Boswell et al., 2019 for MIS 6), and the Red Sea relative sea-level record (Grant et al., 2014); (E) normalised counts of iceberg-rafted detritus (IRD) at MD03–2692 (Mojtahid et al., 2005), and speleothems $\delta^{18}O$ records from Pindal Cave (MIS 2; Moreno et al., 2010), Villars Cave (MIS 4; Genty et al., 2003) and Abaliget Cave (MIS 6; Koltai et al., 2017) (see Fig. 1 for cave locations). Growth hiatuses indicate cold/dry conditions; (F) WDC (MIS 2 and late MIS 4; WAIS Divide Project Members, 2015) and Dome Fuji (MIS 4 and MIS 6; Dome Fuji Ice Core Project Members et al., 2017) $\delta^{18}O$ records of Antarctica ice, and the composite CO_2 record (Ahn and Brook, 2014; Bereiter et al., 2012; Marcott et al., 2014; Petit et al., 1999; Schneider et al., 2013). HS: Heinrich stadials (including HQ, see Bassis et al., 2017 and Zhou et al., 2021). (For interpretation of the references to colour in this figure legend, the reader is referred to the web version of this article.)

Table 4
Mean neodymium isotope signature (expressed in εNd) of Middle-Late Pleistocene glacigenic sediments (< 63 μm; $n = 56$) collected along the southern margins of the British-Irish (BIIS) and Fennoscandian (FIS) ice sheets (Boswell et al., 2018, 2019; Toucanne et al., 2015). Geographic clusters correspond to potential sediment sources at sites MD95–2002 and MD13–3438 according to LGM (and LGM-like) palaeogeography in Western Europe (Fig. 1), as follows: SE Ireland (western BIIS – ISIS; $n = 5$) = Ballycrooneen, Ardmore Bay, Whitting Bay, Killiney Bay, Skerries (from West to East; O'Cofaigh and Evans, 2007); East UK and North Sea (eastern BIIS – western FIS; $n = 6$) = Filey Bay, Happisburg, Dogger Bank (*e.g.* Carr et al., 2000; Evans and Thomson, 2010); North European Plain – West (southwestern FIS; $n = 19$) = Knud Strand, Rubjerg Knude, Karup, Røjle, Trelde Næs, Ashoved, Trävermunde, Beelitz, Althüttendorf, Macherlust (*e.g.* Lüthgens and Böse, 2011; Pedersen, 2005); North European Plain – East (southern FIS; $n = 26$) = Hetmanice, Karchowo, Gorzen, Trzciniec, Wypaleniska, Kozlowo, Chrostkowo, Rogowiec, Szczercόw, Oborki, Glaznoty (*e.g.* Krzyszkowski et al., 1999; Weckwerth, 2010). Note that the mean εNd signatures for SE Ireland and East UK - North Sea do not include the (outlier) samples from Kilmore Quay (KQE1) and Dogger Bank (BGS11), respectively. Depositional environments and stratigraphy (with associated references) are detailed in Toucanne et al. (2015) and Boswell et al. (2019).

Geographic EIS clusters	Country (Longitude)	Samples (n=)	εNd	±	2 sd
SE Ireland (southwestern BIIS - ISIS)	Ireland (8.1–6.1°W)	5	−11.8	±	0.7
East UK and North Sea (eastern BIIS - western FIS)	UK (0.3°W - 2.2°E)	6	−13.1	±	0.6
North European Plain - West (southwestern FIS)	Denmark, Germany (8.7–13.8°E)	19	−14.2	±	1.5
North European Plain - East (southern FIS)	Poland (16.2–19.4°E)	26	−14.8	±	0.8

northern Bay of Biscay ($\leq$ 35 g cm^2 kyr^{-1} and $\leq$ 0.23, respectively) compared to MIS 2 (up to 200 g cm^2 kyr^{-1} and 0.65, respectively) (Fig. 4).

The lack of Baltic-type εNd signals in the northern Bay of Biscay during MIS 4 has profound palaeoenvironmental implications. It indicates, in particular, that during MIS 4, the FIS meltwater and huge river systems from the North European Plain (*i.e.* Oder, Vistula, Daugava) never drained into the Channel River system. As a result, our data indicate that the eastern BIIS and western FIS ice lobes were not sufficient in extent and volume to form a grounded ice bridge (ice saddle) onto the North Sea, the latter being required for river systems east of the North Sea to be diverted to the Bay of Biscay (Gibbard, 1988; Patton et al., 2017). Thus, it is hypothesised that FIS meltwater and North European Plain rivers drained northward into the Nordic Seas. This could have happened beneath the ice if the coalescent (thin) ice lobes were floating, or more likely (considering the lowstand conditions) through a terrestrial corridor (similar to the Ling Bank drainage channel *ca.* 19–17 ka; Sejrup et al., 2016) between the opposing grounded ice lobes reported in the Witch Ground basin and in the Norwegian Channel (Carr et al., 2006; Graham et al., 2011; Mangerud, 2004; Sejrup et al., 2000). The presence of such a corridor and the associated drainage route could explain the planktic $\delta^{18}O$ evidence at the northern North Sea margin (site MD99–2283; Fig. 1) for fresher and/or warmer surface water during MIS 4 compared to the LGM when the North Sea was covered by ice ($\delta^{18}O$ values 0.2–0.4‰ higher at *ca.* 30–20 ka; Lekens et al., 2009). Unfortunately, there are no planktic $\delta^{18}O$ values at site MD99–2283 (Lekens et al., 2009) for the time interval when the BIIS and FIS unzipped *ca.* 19–17 ka (Hughes et al., 2016a; Sejrup et al., 2016), preventing this hypothesis from being explored further. Nevertheless, findings from the Western European margin suggest that glaciation in Western Europe during MIS 4 was less significant than glaciation during MIS 6 (Drenthe Stadial) and MIS 2 (LGM), when grounded ice covered the North Sea and caused FIS meltwater to flow into the Bay of Biscay. This interpretation is supported by the lack of evidence for MIS 4 glaciation in the southern North Sea (Gibbard et al., 2022; Laban and van der Meer, 2011), as well as the fact that most relics of this glaciation in Northern Central Europe (*i.e.* Germany, Poland and Lithuania; Marks et al., 2022) and on the Mid-Norwegian continental margin (Sejrup et al., 2005; Sejrup and Hjelstuen, 2022) are within MIS 6 and MIS 2 glacial limits and were buried by FIS-derived sediments during the LGM ice advance. Loess-palaeosol characteristics (facies succession, loess thickness, structures and mineralogy) in western Germany, Belgium and northern France likewise differ significantly between MIS 6–2 and MIS 4. Loess accumulations are 4 to 5 times finer during MIS 4 than during MIS 6 and MIS 2, indicating lower ice volume and no damming in the North Sea basin (Antoine et al., 2016, 2021). Thus, the findings presented here call to question previous numerical and data-based reconstructions that conclude for a North Sea glaciation during MIS 4 (Batchelor et al., 2019; Gowan et al., 2021; Greenwood et al., 2022). Data-based reconstructions primarily rely on the conclusions of Carr et al. (2006) from a study on buried North Sea sediments. However, these authors emphasise that their reconstruction « *should be considered tentative at best* » because of the ambiguous status, in nature and stratigraphy, of the formations they studied (*i.e.* Ferder and Coal Pit Formations at 58–61°N).

It is difficult to estimate the significance, in ice volume and sea-level equivalent, of our conclusion. The numerical simulations of global ice-sheet reconstructions (at 2.5 kyr-resolution) by Gowan et al. (2021) could help consider that they produce a transition from a narrow ice-free corridor to a grounded ice bridge over the North Sea twice over the last glacial cycle (at 62.5–60 ka and 22.5–20 ka). Such palaeogeographical changes occur at 40-ky intervals, under different climatic conditions, and imply increases in ice volume of similar magnitude of 0.6–0.8 × 10^6 m^3, or 1.6–1.9 m sea-level equivalent (Gowan et al., 2021). This change represents up to 2% of the eustatic sea level at MIS 4 (−97 to −103 m at 64 ka; Grant et al., 2014). This change in ice volume, added to the consequence of a meltwater routing scenario (*i.e.* directly into or upstream to the Nordic seas) on thermohaline circulation (Roche et al., 2010; Toucanne et al., 2021), strongly highlights the need to accurately constrain regional ice-sheet patterns.

5.2. *New insights into the southwestern BIIS during MIS 4*

5.2.1. *Evidence for ice-margin fluctuations in the Celtic-Irish Sea during MIS 4*

The above findings suggest that northern Bay of Biscay sediment dating from MIS 4 was non-Baltic in origin. Here, it is proposed that part of this sediment could originate from the north of the Bay of Biscay and the southwestern British Isles, especially during GS-19.1 *ca.* 68–65 ka. For that period in time, sediment at MD95–2002/MD13–3438 is characterised by a substantial decrease in εNd (down to −12.2), a peak in BIT-index (up to 0.23) and kaolinite content (up to 20%) and illite crystallinity (ICr) increasing from 0.26 to 0.33 to 0.41 (Figs. 3 and 4). Such ICr values indicate that illite during GS-19.1 no longer originates from source(s) characterised by low-grade metamorphic, anchizonal conditions (*i.e.* lower greenschist facies), but through diagenesis processes (Kubler, 1967; Kübler and Jaboyedoff, 2000). Greenschist facies in Western Europe are widely associated with the Variscan belt in which Palaeozoic sediment has suffered from deformation as a result of orogenic activity (*e.g.* the Rhine graben/Rhenish Massif, with ICr down to 0.2; Hueck et al., 2022). Cornwall and southwest Ireland (North Variscan domain), the Armorican Massif in northwest France (Central Variscan domain) and the Iberian Massif in northern Spain (South Variscan domain; Edel et al., 2018) all provide metamorphic illite (ICr $\leq$ 0.3) to the Bay of Biscay (Gutiérrez-Alonso and Nieto, 1996; Meere, 1995; Primmer, 1985). The substantial flux of metamorphic illite (45–57% of the clay assemblage) at MD13–3438 throughout MIS 4 likely originates from these Variscan regions, and it is speculated by extension,

that surrounding regions (but not the kaolinite-poor North Sea, Irion and Zöllmer, 1999; see Section 5.1) are the cause of the GS-19.1 non-metamorphic sediment excursion. River catchments of the southern Bay of Biscay (*e.g.* Loire, Gironde; Fig. 1) are excluded because of their 'high' εNd signatures ($-11 < \varepsilon Nd < -8$; Bayon et al., 2015; Parra et al., 1998), as well as the Seine and Rhine basins of the Channel River that produce smectite-rich sediments (63% and 52%, respectively; Bayon et al., 2015). Conversely, the mid- to late Palaeozoic formations of Northern Cornwall, South Wales (Upper Carboniferous; Primmer, 1985; Warr et al., 1991) and the Welsh Borderland (Silurian; Robinson and Bevins, 1986) produce diagenetic illite, together with kaolinite (Allen, 1991; Primmer, 1985; Teale and Spears, 1986), that both characterise the clay assemblage of the Welsh mountains (Battiau-Queney, 1984). Until 20–19 ka, the Welsh mountains hosted the >1000-m-thick Welsh Ice Cap (Hughes et al., 2022a; Hughes et al., 2016b), subsumed by the BIIS and fuelling the Irish Sea Ice Stream (ISIS) that extended down through the Celtic-Irish Sea at least as far as Lundy Island (51°N, *ca.* 400 km north of site MD13–3438) during MIS 4 (Gibbard et al., 2017; Hughes et al., 2022a; Rolfe et al., 2012). Thus, the change in sediment composition at MD13–3438 during GS-19.1 likely originates from this source region, and specifically from ISIS activity. It is interesting to note that the Mullaghareik mountains (Ireland), Southern Uplands (Scotland), Lake District and Northern Pennines (England; Fig. 1), that hosted additional ice centres of the western BIIS, are composed of mid- to late Palaeozoic formations that resemble those of Northern Cornwall and Wales (see Fortey et al., 1993 and Merriman et al., 1995 for ICr values). Rocks from these regions provide heterogenous εNd (Davies et al., 1985; Stone and Evans, 2000). In contrast, river sediments, because they correlate with the mean age and isotopic signature from drainage basins (Goldstein and Jacobsen, 1988), give εNd values with a compact range of -12.4 ± 0.3 for the Blackwater (Ireland), Severn, Trent and Ouse rivers (central England and Wales) that all drain from the Palaeozoic formations of the central British Isles (Bayon et al., 2015; Toucanne et al., 2015). These values, as well as those of LGM glacigenic sediments from southeast Ireland (11.8 ± 0.7; Table 4), are close to those found for the GS-19.1 sediment at MD13–3438, and confirm that the Celtic-Irish Sea region, *via* the ISIS, was the likely source for northern Bay of Biscay sediment at that time.

The mobilisation and transport of BIIS-derived sediments to the northern Bay of Biscay during GS-19.1 required sediment availability and enhanced meltwater production, two conditions fulfilled by accelerated glacier melt (*e.g.* Church and Ryder, 1972; Delaney and Adhikari, 2020). Thus, the GS-19.1 sediment at MD13–3438 probably highlights a significant ice-margin retreat of the ISIS *ca.* 68–65 ka. This scenario implies a significant build-up of the BIIS in the Celtic-Irish Sea region before *ca.* 68 ka, possibly from *ca.* 72–71 ka as suggested by the strong regional air-sea thermal contrast (Sánchez Goñi et al., 2013) and the rapid decrease in eustatic sea level (Grant et al., 2014). Such a timing is consistent firstly with the arrival of diagnostic BIIS IRD northwest of Ireland (site MD04–2822; Fig. 1) as early as *ca.* 70 ka, indicating that the western BIIS reached the ocean at that time (Hibbert et al., 2010), and secondly, with MIS 2 constraints for the ISIS that rapidly grew from the mountains (53°N; *ca.* 31 ka) to close to the continental shelf break (49°N; *ca.* 27 ka) in only about 4 kyr (Clark et al., 2022). It is noteworthy that the MIS 4 IRD flux offshore Ireland (MD04–2822) is 2 to 6 times lower than during MIS 2 (Hibbert et al., 2010), thus suggesting, in the same way as for the North Sea (Section 5.1), that the ice volume over the British Isles during MIS 4 was lower than during MIS 2 (except locally where ice volumes were thicker over some mountain areas such as Wales; *e.g.* Hughes et al., 2022a).

5.2.2. *Early retreat of the southwestern BIIS during MIS 4 and comparison with the post-LGM retreat*

The MIS 4 ISIS retreat at *ca.* 68–65 ka occurred well before the MIS 4–3 transition and the associated deglaciation (*ca.* 64–60 ka) testified by the concomitant ~35-m eustatic sea-level rise (Grant et al., 2014; Waelbroeck et al., 2002b; Figs. 4 and 5). The latter, occurring throughout HS 6, was likely forced by enhanced boreal summer insolation and atmospheric CO_2. It is interesting to note that similar conditions in boreal summer insolation (490–520 W m^{-2} at 45°N) and atmospheric CO_2 (*ca.* 20–40 ppm increases) characterise both HS 6 and the massive deglacial FIS retreat events of HS 12 (MIS 6, *ca.* 155 ka) and HS 1 (18–17 ka) (Fig. 4). Thus, by drawing an analogy between these events, HS 6 can be considered as a global deglacial period (or 'unfinished termination'; see Dalton et al., 2022 and Schaefer et al., 2015) and the FIS melting, although not recorded in the Bay of Biscay (see Section 5.1), likely contributed to the HS 6 sea-level rise (Lambeck et al., 2010; Siegert et al., 2001; Svendsen et al., 2004; Salonen et al., 2008). This climate scenario for MIS 4 highlights how early the ISIS retreat was.

The timing of the ISIS retreat during MIS 4 resembles that of MIS 2. Indeed, the last ISIS reached its maximum extent into the Celtic Sea at *ca.* 27–26 ka and rapidly receded, together with the ice streams of northwest Ireland (Callard et al., 2018; O'Cofaigh et al., 2019), at *ca.* 26–24 ka (Clark et al., 2022). This retreat is early for the EIS as a whole for which deglaciation started at *ca.* 21 ka and strongly accelerated during HS 1 (Hughes et al., 2016a; Ménot et al., 2006; Zaragosi et al., 2001). Hence, the periods of ISIS retreat during MIS 4 (*ca.* 68–65 ka) and MIS 2 (*ca.* 26–24 ka) precedes in both cases the onset of the (unfinished or full) global deglaciation (*ca.* 64 ka and *ca.* 21 ka, respectively) by a few millennia (Fig. 5). This time lapse is highlighted by short-term interstadial warming periods (GI-18 and GI-2) favourable to EIS growth (Sánchez Goñi et al., 2013). Also, both the ISIS retreat and the subsequent rapid deglaciation during MIS 4 and MIS 2 coincide with HS conditions, *i.e.* strong North Atlantic sea-surface and atmospheric cooling testified by pollen (*i.e.* expansion of semi-desert taxa; Fig. 3) and speleothem records over Western Europe (Fig. 4), and the high content of polar planktonic foraminifera and IRD in the Bay of Biscay and eastern North Atlantic sediment (Fig. 3). Indeed, in MIS 4, the ISIS retreat occurred during the so-called HQ and preceded global deglaciation which is coeval with HS 6. In MIS 2, the ISIS retreat is coeval with HS 2 (*e.g.* Scourse et al., 2000) and preceded the global deglaciation that dramatically accelerated during HS 1 (Fig. 5). This pattern of unexpected ice-sheet retreat during HS conditions (see Toucanne et al., 2015 for HS 1, HS 2 and HS 3) reinforces, together with concomitant evidence for warmer sea-surface conditions in the mid-latitude central North Atlantic (Naafs et al., 2013) and the Norwegian Sea (Wary et al., 2017), the Heinrich summer hypothesis of Denton et al. (2022). These authors emphasised extreme seasonality during HS, with warmer-than-usual summers on continental ice sheets adjacent to the North Atlantic that led to discharges of meltwater and icebergs of sufficient volume to stimulate very cold winter conditions from widespread sea ice on a freshened ocean surface. This hypothesis postulates that the causative variations in freshwater fluxes were driven by a climate signal most evident in Antarctic ice cores. The early ISIS retreats discussed here are coeval with Antartic warming episodes and *ca.* 10–20 ppm atmospheric CO_2 rises (Fig. 5), and are likely strengthened by obliquity (from 22.5 to 23°), that increased as soon as *ca.* 70 ka and *ca.* 29 ka (Fig. 5). Increases in obliquity cause symmetric, sustained increases in intensity (together with CO_2) and duration of summer at latitudes above 40° in both hemispheres, and hence control the temperate and high-latitude ice-sheet (including BIIS) mass balance. Consequently, obliquity is considered to be a strong forcing on deglaciation (Bajo et al., 2020; Huybers, 2007; Huybers and Denton, 2008). It is consequently presumed that the MIS 4 ISIS retreat during HQ likely originates from enhanced surface melt in response to regional sustained changes in summer conditions (intensity, duration). The increase in oceanic subsurface (≥150 m depth) temperature associated with the HS conditions (Marcott et al., 2011; Max et al., 2022) could also have favoured the ice retreat, but only if the ISIS was marine-based. Local sea-level rise, as well as topographical factors, have been widely explored over these last years to explain the last retreat of the ISIS and neighbouring ice streams, that all were marine-based at *ca.* 27–26 ka (see Clark et al., 2022 for a thorough

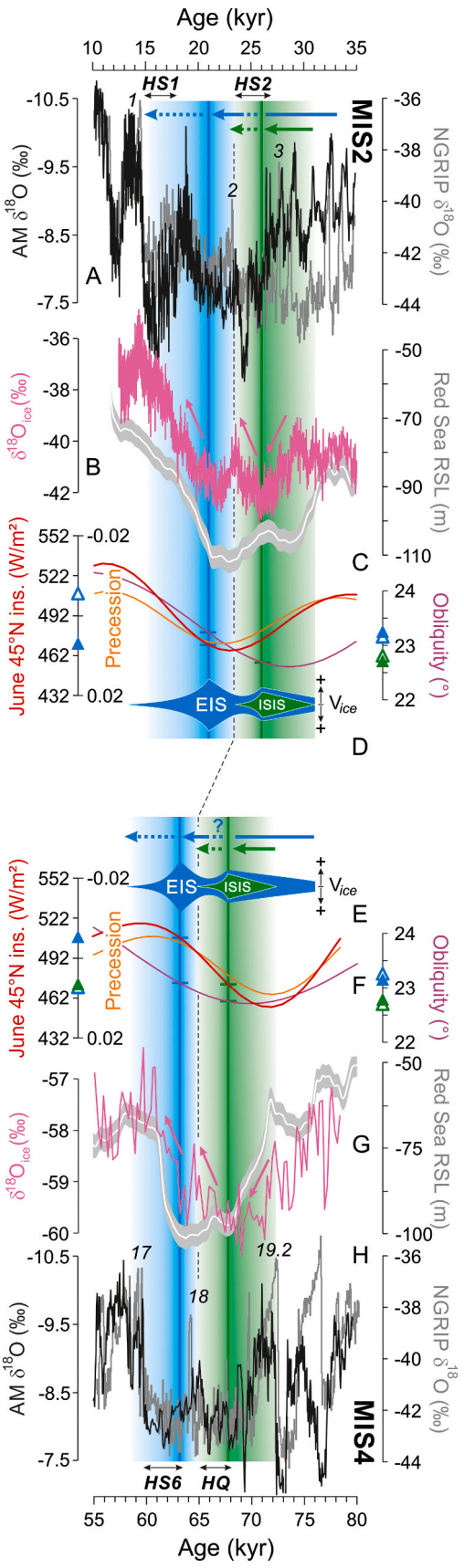

(caption on next column)

Fig. 5. (A, H) The composite AM $\delta^{18}O$ record (Cheng et al., 2016) and the NGRIP $\delta^{18}O$ record (GICC05 modelext timescale; Rasmussen et al., 2014; Seierstad et al., 2014); (B, G) $\delta^{18}O$ records of Antarctica ice (Dome Fuji Ice Core Project Members et al., 2017; WAIS Divide Project Members, 2015), and the Red Sea relative sea-level record (Grant et al., 2014); (C, F) June insolation at 45°N, and the precession and obliquity (Laskar et al., 2004). The coloured (full) triangles on the insolation/obliquity scale highlight the insolation/obliquity forcing corresponding to the onset of ice-margin retreat for both the EIS (blue) and ISIS (green). Open triangles in the MIS 2 panel correspond to the full triangles in the MIS 4 panel, and *vice-versa*; (D, E) Schematic evolution of the EIS and ISIS volume/extent for MIS 2 (D) and MIS 4 (E), consistent with the continuous (ice advance) and dashed (ice retreat) arrows at the top of each panel (blue arrows: EIS; green arrows: ISIS). See the main text for details. The vertical blue/green bands highlight the evolution of the EIS/ISIS, respectively. The vertical (continuous, coloured) lines show the LGM (−like) conditions for the EIS/ISIS. HS: Heinrich stadials (including HQ, see Bassis et al., 2017 and Zhou et al., 2021).

review). These factors are of primary importance, but the palaeoclimatic constraints for MIS 4 ISIS fluctuations, together with MIS 2, strongly emphasise the role of climate (obliquity) forcing, and HS conditions in particular, on the ISIS behaviour. This is in line with the very southern position of the ISIS ice centres (53–55°N) and their close proximity to the ocean and the North Atlantic Drift current, that necessarily make the ISIS (and more generally the BIIS; Peck et al., 2006) a very sensitive portion of the EIS and, by extension, a sentinel of climate and ice-sheet changes in the eastern North Atlantic region.

6. Conclusions

The sediments of the northern Bay of Biscay provide insight into the drainage and dynamics of the Western EIS during MIS 4. Their study reveals the absence of Baltic-derived material in the Bay of Biscay throughout MIS 4, which indicate that the routing of FIS meltwater into the NE Atlantic *via* the Channel River, reported for the Late Saalian MIS 6 (Drenthe Stadial) and the Late Weichselian LGM (during MIS 2), did not occur during the Middle Weichselian MIS 4 glaciation. This indicates a limited Channel River catchment, likely centred on northern France and the southern British Isles, and excludes the North European Plain and the southern Baltic region, that constituted the upstream sources of the Channel River system when the BIIS and FIS coalesced into the North Sea. Thus, it is supposed that the BIIS and FIS did not form a grounded ice bridge onto the North Sea during MIS 4 and, by extension, that the MIS 4 glaciation in Western Europe was relatively limited in comparison to those of MIS 6 and MIS 2, although with some regional and local exceptions such as over Wales in the British Isles. These findings balance the recent conclusions of Doughty et al. (2021) in placing MIS 4 as a medium-scale glacial event, at least in Western Europe.

The MIS 4 drainage configuration, and more precisely the absence of huge inputs of Baltic material, also allowed southwestern BIIS fluctuations to be recorded (*i.e.* not diluted) in the northern Bay of Biscay sediments. MD13–3438 data suggest ice-marginal retreat in the Celtic-Irish Sea sector as soon as *ca.* 68–65 ka (HQ), a few millennia before the demise of the EIS (*ca.* 64–60 ka, HS 6). This timing resembles that described for the LGM, highlighting the southwestern BIIS as a sentinel of climate changes in the NE Atlantic. It is noteworthy that the successive local (BIIS) and regional (EIS) retreats, both during MIS 4 and MIS 2, are coeval with increasing obliquity. Thus, they each likely result from increasing summer duration that in turn promotes ice melting and increases meltwater flux to the ocean. The latter, in stimulating cold winter conditions from widespread sea ice, likely explains the HS conditions with which the successive MIS 4 and MIS 2 ice-margin retreats coincide. Thus, as for MIS 2 (Denton et al., 2010, 2022), the MIS 4 interval corresponds to a complex combination of general ice advance interspersed by preliminary-to-final EIS demises highlighted by HS conditions.

Declaration of Competing Interest

The authors declare the following financial interests/personal relationships which may be considered as potential competing interests:

Teresa Rodrigues reports financial support was provided by Portuguese Institute for the Sea and Atmosphere. Jaap S. SINNINGHE DAMSTE reports financial support was provided by NIOZ Royal Institute for Sea Research. Frederique Eynaud reports financial support was provided by Univ. Bordeaux, CNRS, Bordeaux INP, EPOC, UMR 5805.

Data availability

Data will be made available on request.

Acknowledgments

Authors are grateful to M. Wary (EPOC) for assistance during XRF scanning, L. Sanchi (CEREGE) for biomarker analyses, M. Pitel-Roudault (IFREMER) for mapping, G. Bayon and A. Trinquier (IFREMER) for assistance during MC-ICPMS analyses, A. Chalm (IFREMER) for language improvements and the two reviewers for their helpful comments on the manuscript. T. Rodrigues acknowledges funding from Portuguese FCT -Foundation for Science and Technology- through projects WarmWorld (PTDC/CTA-GEO/29897/2017), Hydroshyft (PTDC/CTA-CLI/4608/2020, UIDB/04326/2020, LA/P/0101/2020), and EMSO-PT (POCI-01-0145-FEDER-022157). F. Eynaud acknowledges supports from the French project INSU ICE-BIO-RAM and by the European Research Council ERC grant ACCLIMATE/n° 339108, that provided funding for the study of core MD13-3438 in the frame of the post-doctoral project of W. Fersi (under the coordination of A. Penaud). The work of J. S. Sinninghe Damsté was supported by a grant from the Nederlandse Organisatie voor Wetenschappelijk Onderzoek (n°024.002.001) from the Dutch Ministry for Education, Culture and Science.

References

Ahn, J., Brook, E.J., 2014. Siple Dome ice reveals two modes of millennial CO2 change during the last ice age. Nat. Commun. 5, 1–6.

Allard, J.L., Hughes, P.D., Woodward, J.C., 2021. A radiometric dating revolution and the Quaternary glacial history of the Mediterranean mountains. Earth Sci. Rev. 223, 103844.

Allen, J., 1991. Fine sediment and its sources, Severn Estuary and inner Bristol Channel, southwest Britain. Sediment. Geol. 75, 57–65.

Antoine, P., Coutard, J., Gibbard, P., Hallegouet, B., Lautridou, J., Ozouf, J., 2003. The Pleistocene rivers of the English Channel region. J. Quat. Sci.: Publ. Quat. Res. Assoc. 18, 227–243.

Antoine, P., Guerin, G., Deschodt, L., Goval, E., Locht, J.-L., Paris, C., 2016. Upper Pleistocene loess-palaeosol records from Northern France in the European context: environmental background and dating of the Middle Palaeolithic. Quat. Int. 411, 4–24.

Antoine, P., Coutard, S., Bahain, J., Locht, J., Hérisson, D., Goval, E., 2021. The last 750 ka in loess–palaeosol sequences from northern France: environmental background and dating of the western European Palaeolithic. J. Quat. Sci. 36, 1293–1310.

Auffret, G., Zaragosi, S., Dennielou, B., Cortijo, E., Van Rooij, D., Grousset, F., Pujol, C., Eynaud, F., Siegert, M., 2002. Terrigenous fluxes at the Celtic margin during the last glacial cycle. Mar. Geol. 188, 79–108.

Bajo, P., Drysdale, R.N., Woodhead, J.D., Hellstrom, J.C., Hodell, D., Ferretti, P., Voelker, A.H., Zanchetta, G., Rodrigues, T., Wolff, E., 2020. Persistent influence of obliquity on ice age terminations since the Middle Pleistocene transition. Science 367, 1235–1239.

Balco, G., 2020. Glacier change and paleoclimate applications of cosmogenic-nuclide exposure dating. Annu. Rev. Earth Planet. Sci. 48, 21–48. https://doi.org/10.1146/annurev-earth-081619-052609.

Barker, S., Diz, P., Vautravers, M.J., Pike, J., Knorr, G., Hall, I.R., Broecker, W.S., 2009. Interhemispheric Atlantic seesaw response during the last deglaciation. Nature 457, 1097–1102.

Bassis, J.N., Petersen, S.V., Mac Cathles, L., 2017. Heinrich events triggered by ocean forcing and modulated by isostatic adjustment. Nature 542, 332–334.

Batchelor, C.L., Margold, M., Krapp, M., Murton, D.K., Dalton, A.S., Gibbard, P.L., Stokes, C.R., Murton, J.B., Manica, A., 2019. The configuration of Northern Hemisphere ice sheets through the Quaternary. Nat. Commun. 10, 1–10.

Battiau-Queney, Y., 1984. The pre-glacial evolution of Wales. Earth Surf. Process. Landf. 9, 229–252.

Bayon, G., German, C., Boella, R., Milton, J., Taylor, R., Nesbitt, R., 2002. An improved method for extracting marine sediment fractions and its application to Sr and Nd isotopic analysis. Chem. Geol. 187, 179–199.

Bayon, G., Barrat, J.A., Etoubleau, J., Benoit, M., Bollinger, C., Révillon, S., 2009. Determination of rare earth elements, Sc, Y, Zr, Ba, Hf and Th in geological samples by ICP-MS after Tm addition and alkaline fusion. Geostand. Geoanal. Res. 33, 51–62.

Bayon, G., Toucanne, S., Skonieczny, C., André, L., Bermell, S., Cheron, S., Dennielou, B., Etoubleau, J., Freslon, N., Gauchery, T., 2015. Rare earth elements and neodymium isotopes in world river sediments revisited. Geochim. Cosmochim. Acta 170, 17–38.

Bereiter, B., Lüthi, D., Siegrist, M., Schüpbach, S., Stocker, T.F., Fischer, H., 2012. Mode change of millennial CO2 variability during the last glacial cycle associated with a bipolar marine carbon seesaw. Proc. Natl. Acad. Sci. 109, 9755–9760.

Blaauw, M., Christen, J.A., 2011. Flexible paleoclimate age-depth models using an autoregressive gamma process. Bayesian Anal. 6, 457–474.

Boswell, S.M., Toucanne, S., Creyts, T.T., Hemming, S.R., 2018. Continental-scale transport of sediments by the Baltic ice stream elucidated by coupled grain size and Nd provenance analyses. Earth Planet. Sci. Lett. 490, 143–150.

Boswell, S.M., Toucanne, S., Pitel-Roudaut, M., Creyts, T.T., Eynaud, F., Bayon, G., 2019. Enhanced surface melting of the Fennoscandian Ice Sheet during periods of North Atlantic cooling. Geology 47, 664–668.

Bourillet, J.-F., Turon, J.-L., 2003. MD133 / SEDICAR Cruise, RV Marion Dufresne. https://doi.org/10.17600/3200060.

Bourillet, J.-F., Damy, G., Dussud, L., Sultan, N., Woerther, P., Migeon, S., 2007. Behaviour of a piston corer from accelerometers and new insights on quality of the recovery. In: Proceedings of the 6th International Offshore Site Investigation and Geotechnics Conference: Confronting New Challenges and Sharing Knowledge, 11–13 September 2007, London, UK. https://archimer.ifremer.fr/doc/00071/18198/15766.pdf.

Busschers, F., Kasse, C., Van Balen, R., Vandenberghe, J., Cohen, K., Weerts, H., Wallinga, J., Johns, C., Cleveringa, P., Bunnik, F., 2007. Late Pleistocene evolution of the Rhine-Meuse system in the southern North Sea basin: imprints of climate change, sea-level oscillation and glacio-isostacy. Quat. Sci. Rev. 26, 3216–3248.

Butzin, M., Prange, M., Lohmann, G., 2005. Radiocarbon simulations for the glacial ocean: the effects of wind stress, Southern Ocean sea ice and Heinrich events. Earth Planet. Sci. Lett. 235, 45–61.

Callard, S.L., Cofaigh, C.Ó., Benetti, S., Chiverrell, R.C., Van Landeghem, K.J., Saher, M. H., Gales, J.A., Small, D., Clark, C.D., Stephen, J.L., 2018. Extent and retreat history of the Barra fan ice stream offshore western Scotland and northern Ireland during the last glaciation. Quat. Sci. Rev. 201, 280–302.

Carr, S.J., Haflidason, H., Sejrup, H.P., 2000. Micromorphological evidence supporting Late Weichselian glaciation of the northern North Sea. Boreas 29, 315–328.

Carr, S., van der Holmes, R., Van der Meer, J., Rose, J., 2006. The Last Glacial Maximum in the North Sea Basin: micromorphological evidence of extensive glaciation. J. Quat. Sci. 21, 131–153.

Chamley, H., 1989. Clay Mineralogy.

Cheng, H., Edwards, R.L., Wang, Y., Kong, X., Ming, Y., Kelly, M.J., Wang, X., Gallup, C. D., Liu, W., 2006. A penultimate glacial monsoon record from Hulu Cave and two-phase glacial terminations. Geology 34, 217–220.

Cheng, H., Edwards, R.L., Sinha, A., Spötl, C., Yi, L., Chen, S., Kelly, M., Kathayat, G., Wang, X., Li, X., 2016. The Asian monsoon over the past 640,000 years and ice age terminations. Nature 534, 640–646.

Cheng, H., Edwards, R.L., Southon, J., Matsumoto, K., Feinberg, J.M., Sinha, A., Zhou, W., Li, H., Li, X., Xu, Y., 2018. Atmospheric 14C/12C changes during the last glacial period from Hulu Cave. Science 362, 1293–1297.

Christen, J.A., Pérez, S., 2009. A new robust statistical model for radiocarbon data. Radiocarbon 51, 1047–1059.

Church, M., Ryder, J.M., 1972. Paraglacial sedimentation: a consideration of fluvial processes conditioned by glaciation. Geol. Soc. Am. Bull. 83, 3059–3072.

Clark, P.U., Dyke, A.S., Shakun, J.D., Carlson, A.E., Clark, J., Wohlfarth, B., Mitrovica, J. X., Hostetler, S.W., McCabe, A.M., 2009. The last glacial maximum. Science 325, 710–714.

Clark, C.D., Ely, J.C., Hindmarsh, R.C., Bradley, S., Ignéczi, A., Fabel, D., Cofaigh, C.Ó., Chiverrell, R.C., Scourse, J., Benetti, S., 2022. Growth and retreat of the last British–Irish Ice Sheet, 31 000 to 15 000 years ago: the BRITICE-CHRONO reconstruction. Boreas 51, 699–758.

Cofaigh, Ó.C., Telfer, M.W., Bailey, R.M., Evans, D.J., 2012. Late Pleistocene chronostratigraphy and ice sheet limits, southern Ireland. Quat. Sci. Rev. 44, 160–179.

Colville, E.J., Carlson, A.E., Beard, B.L., Hatfield, R.G., Stoner, J.S., Reyes, A.V., Ullman, D.J., 2011. Sr-Nd-Pb isotope evidence for ice-sheet presence on southern Greenland during the Last Interglacial. Science 333, 620–623.

Corrick, E.C., Drysdale, R.N., Hellstrom, J.C., Capron, E., Rasmussen, S.O., Zhang, X., Fleitmann, D., Couchoud, I., Wolff, E., 2020. Synchronous timing of abrupt climate changes during the last glacial period. Science 369, 963–969.

Cotterill, C.J., Phillips, E., James, L., Forsberg, C.F., Tjelta, T.I., Carter, G., Dove, D., 2017. The evolution of the Dogger Bank, North Sea: a complex history of terrestrial, glacial and marine environmental change. Quat. Sci. Rev. 171, 136–153.

Cutler, K., Edwards, R., Taylor, F., Cheng, H., Adkins, J., Gallup, C., Cutler, P., Burr, G., Bloom, A., 2003. Rapid sea-level fall and deep-ocean temperature change since the last interglacial period. Earth Planet. Sci. Lett. 206, 253–271.

Dalton, A.S., Margold, M., Stokes, C.R., Tarasov, L., Dyke, A.S., Adams, R.S., Allard, S., Arends, H.E., Atkinson, N., Attig, J.W., 2020. An updated radiocarbon-based ice margin chronology for the last deglaciation of the North American ice sheet complex. Quat. Sci. Rev. 234, 106223.

Dalton, A.S., Stokes, C.R., Batchelor, C.L., 2022. Evolution of the Laurentide and Innuitian ice sheets prior to the Last Glacial Maximum (115 ka to 25 ka). Earth Sci. Rev. 224, 103875.
Davies, G., Gledhill, A., Hawkesworth, C., 1985. Upper crustal recycling in southern Britain: evidence from Nd and Sr isotopes. Earth Planet. Sci. Lett. 75, 1–12.
De Jonge, C., Stadnitskaia, A., Hopmans, E.C., Cherkashov, G., Fedotov, A., Sinninghe Damsté, J.S., 2014. In situ produced branched glycerol dialkyl glycerol tetraethers in suspended particulate matter from the Yenisei River, Eastern Siberia. Geochim. Cosmochim. Acta 125, 476–491.
Delaney, I., Adhikari, S., 2020. Increased subglacial sediment discharge in a warming climate: consideration of ice dynamics, glacial erosion, and fluvial sediment transport. Geophys. Res. Lett. 47 e2019GL085672.
Denton, G.H., Anderson, R.F., Toggweiler, J.R., Edwards, R.L., Schaefer, J.M., Putnam, A. E., 2010. The last glacial termination. Science 328, 1652–1656.
Denton, G.H., Toucanne, S., Putnam, A.E., Barrell, D.J., Russell, J.L., 2022. Heinrich summers. Quat. Sci. Rev. 295, 107750.
Dome Fuji Ice Core Project Members, Kawamura, K., Abe-Ouchi, A., Motoyama, H., Ageta, Y., Aoki, S., Azuma, N., Fujii, Y., Fujita, K., Fujita, S., 2017. State dependence of climatic instability over the past 720,000 years from Antarctic ice cores and climate modeling. Sci. Adv. 3, e1600446.
Dosseto, A., Hesse, P.P., Maher, K., Fryirs, K., Turner, S., 2010. Climatic and vegetation control on sediment dynamics during the last glacial cycle. Geology 38 (5), 395–398.
Doughty, A.M., Kaplan, M.R., Peltier, C., Barker, S., 2021. A maximum in global glacier extent during MIS 4. Quat. Sci. Rev. 261, 106948.
Edel, J.B., Schulmann, K., Lexa, O., Lardeaux, J.M., 2018. Late Palaeozoic palaeomagnetic and tectonic constraints for amalgamation of Pangea supercontinent in the European Variscan belt. Earth Sci. Rev. 177, 589–612.
Eglinton, G., Hamilton, R.J., 1967. Leaf epicuticular waxes: the waxy outer surfaces of most plants display a wide diversity of fine structure and chemical constituents. Science 156, 1322–1335.
Ehlers, J., Gibbard, P.L., 2007. The extent and chronology of Cenozoic global glaciation. Quat. Int. 164, 6–20.
Evans, D.J., Thomson, S.A., 2010. Glacial sediments and landforms of holderness, eastern England: a glacial depositional model for the North Sea lobe of the British–Irish Ice Sheet. Earth Sci. Rev. 101, 147–189.
Evans, D.J., Roberts, D.H., Bateman, M.D., Clark, C.D., Medialdea, A., Callard, L., Grimoldi, E., Chiverrell, R.C., Ely, J., Dove, D., 2021. Retreat dynamics of the eastern sector of the British–Irish Ice Sheet during the last glaciation. J. Quat. Sci. 36, 723–751.
Eynaud, F., Zaragosi, S., Scourse, J., Mojtahid, M., Bourillet, J.-F., Hall, I.R., Penaud, A., Locascio, M., Reijonen, A., 2007. Deglacial laminated facies on the NW European continental margin: the hydrographic significance of British-Irish Ice Sheet deglaciation and Fleuve Manche paleoriver discharges. Geochem. Geophys. Geosyst. 8.
Faivre, S., Bakran-Petricioli, T., Barešić, J., Morhange, C., Borković, D., 2019. Marine radiocarbon reservoir age of the coralline intertidal alga Lithophyllum byssoides in the Mediterranean. Quat. Geochronol. 51, 15–23.
Fersi, W., Penaud, A., Wary, M., Toucanne, S., Waelbroeck, C., Rossignol, L., Eynaud, F., 2021. Imprint of seasonality changes on fluvio-glacial dynamics across Heinrich Stadial 1 (NE Atlantic Ocean). Glob. Planet. Chang. 204, 103552.
Fortey, N., Roberts, B., Hirons, S., 1993. Relationship between metamorphism and structure in the Skiddaw Group, English Lake District. Geol. Mag. 130, 631–638.
Genty, D., Blamart, D., Ouahdi, R., Gilmour, M., Baker, A., Jouzel, J., Van-Exter, S., 2003. Precise dating of Dansgaard–Oeschger climate oscillations in western Europe from stalagmite data. Nature 421, 833–837.
Gibbard, P., 1988. The history of the great northwest European rivers during the past three million years. Philos. Trans. R. Soc. Lond. Ser. B Biol. Sci. 318, 559–602.
Gibbard, P., 1995. The formation of the Strait of Dover. In: Geological Society, 96. Special Publications, London, pp. 15–26.
Gibbard, P.L., Hughes, P.D., Rolfe, C.J., 2017. New insights into the Quaternary evolution of the Bristol Channel, UK. J. Quat. Sci. 32, 564–578.
Gibbard, P.L., Hughes, P.D., Clark, C.D., Glasser, N.F., Tomkins, M.D., 2022. Britain and Ireland: glacial landforms prior to the Last Glacial Maximum. In: European Glacial Landscapes. Elsevier, pp. 245–253.
Gillespie, A., Molnar, P., 1995. Asynchronous maximum advances of mountain and continental glaciers. Rev. Geophys. 33, 311–364.
Goldstein, S.J., Jacobsen, S.B., 1988. Nd and Sr isotopic systematics of river water suspended material: implications for crustal evolution. Earth Planet. Sci. Lett. 87, 249–265.
Govin, A., Riveiros, N.V., Réaud, Y., Waelbroeck, C., Giraudeau, J., 2016. Unprecedented coring performance with the upgraded research vessel Marion Dufresne. Past Glob. Chang. Mag. 24, 27.
Gowan, E.J., Zhang, X., Khosravi, S., Rovere, A., Stocchi, P., Hughes, A.L., Gyllencreutz, R., Mangerud, J., Svendsen, J.-I., Lohmann, G., 2021. A new global ice sheet reconstruction for the past 80 000 years. Nat. Commun. 12, 1–9.
Graham, A., Lonergan, L., Stoker, M., 2007. Evidence for Late Pleistocene ice stream activity in the Witch Ground Basin, central North Sea, from 3D seismic reflection data. Quat. Sci. Rev. 26, 627–643.
Graham, A.G., Stoker, M.S., Lonergan, L., Bradwell, T., Stewart, M.A., 2011. The Pleistocene glaciations of the North Sea basin. In: Developments in Quaternary Sciences. Elsevier, pp. 261–278.
Grant, K., Rohling, E., Ramsey, C.B., Cheng, H., Edwards, R., Florindo, F., Heslop, D., Marra, F., Roberts, A., Tamisiea, M.E., 2014. Sea-level variability over five glacial cycles. Nat. Commun. 5, 1–9.
Greenwood, S.L., Winsborrow, M.C., Hughes, A.L., 2022. The European ice sheet complex. In: European Glacial Landscapes. Elsevier, pp. 29–36.
Grimalt, J., Albaiges, J., 1990. Characterization of the depositional environments of the Ebro Delta (western Mediterranean) by the study of sedimentary lipid markers. Mar. Geol. 95, 207–224.
Grosswald, M., 1980. Late Weichselian ice sheet of northern Eurasia. Quat. Res. 13, 1–32.
Grousset, F.E., Pujol, C., Labeyrie, L., Auffret, G., Boelaert, A., 2000. Were the North Atlantic Heinrich events triggered by the behavior of the European ice sheets? Geology 28, 123–126.
Gutiérrez-Alonso, G., Nieto, F., 1996. White-mica'crystallinity', finite strain and cleavage development across a large Variscan structure, NW Spain. J. Geol. Soc. 153, 287–299.
Harkness, D., 1983. The extent of natural 14 C deficiency in the coastal environment of the United Kingdom. In: Presented at the Proceedings of the First International Symposium 14 C and Archaeology, Groningen, 1981, pp. 351–364.
Heaton, T.J., Köhler, P., Butzin, M., Bard, E., Reimer, R.W., Austin, W.E., Ramsey, C.B., Grootes, P.M., Hughen, K.A., Kromer, B., 2020. Marine20—the marine radiocarbon age calibration curve (0–55,000 cal BP). Radiocarbon 62, 779–820.
Heaton, T.J., Butzin, M., Bard, E., Bronk Ramsey, C., Hughen, K.A., Köhler, P., Reimer, P. J., 2023. Marine radiocarbon calibration in polar regions: a simple approximate approach using marine20. Radiocarbon 1–28. https://doi.org/10.1017/RDC.2023.42.
Hemming, S.R., 2004. Heinrich events: massive late Pleistocene detritus layers of the North Atlantic and their global climate imprint. Rev. Geophys. 42.
Herfort, L., Schouten, S., Boon, J.P., Woltering, M., Baas, M., Weijers, J.W., Sinninghe Damsté, J.S., 2006. Characterization of transport and deposition of terrestrial organic matter in the southern North Sea using the BIT index. Limnol. Oceanogr. 51, 2196–2205.
Hibbert, F.D., Austin, W.E., Leng, M.J., Gatliff, R.W., 2010. British Ice Sheet dynamics inferred from North Atlantic ice-rafted debris records spanning the last 175 000 years. J. Quat. Sci.: Publ. Quat. Res. Assoc. 25, 461–482.
Hijma, M.P., Cohen, K.M., Roebroeks, W., Westerhoff, W.E., Busschers, F.S., 2012. Pleistocene Rhine–Thames landscapes: geological background for hominin occupation of the southern North Sea region. J. Quat. Sci. 27, 17–39.
Hodell, D., Crowhurst, S., Skinner, L., Tzedakis, P.C., Margari, V., Channell, J.E., Kamenov, G., Maclachlan, S., Rothwell, G., 2013. Response of Iberian Margin sediments to orbital and suborbital forcing over the past 420 ka. Paleoceanography 28, 185–199.
Hodell, D., Lourens, L., Crowhurst, S., Konijnendijk, T., Tjallingii, R., Jiménez-Espejo, F., Skinner, L., Tzedakis, P., Members, T.S.S.P., Abrantes, F., 2015. A reference time scale for Site U1385 (Shackleton Site) on the SW Iberian Margin. Glob. Planet. Chang. 133, 49–64.
Hopmans, E.C., Weijers, J.W., Schefuß, E., Herfort, L., Damsté, J.S.S., Schouten, S., 2004. A novel proxy for terrestrial organic matter in sediments based on branched and isoprenoid tetraether lipids. Earth Planet. Sci. Lett. 224, 107–116.
Hopmans, E.C., Schouten, S., Sinninghe Damsté, J.S., 2016. The effect of improved chromatography on GDGT-based palaeoproxies. Org. Geochem. 93, 1–6.
Hueck, M., Wemmer, K., Ksienzyk, A.K., Kuehn, R., Vogel, N., 2022. Potential, premises, and pitfalls of interpreting illite argon dates-a case study from the German Variscides. Earth Sci. Rev. 104133.
Hughes, A.L., Gyllencreutz, R., Lohne, Ø.S., Mangerud, J., Svendsen, J.I., 2016a. The last Eurasian ice sheets–a chronological database and time-slice reconstruction, DATED-1. Boreas 45, 1–45.
Hughes, P.D., Glasser, N.F., Fink, D., 2016b. Rapid thinning of the Welsh Ice Cap at 20–19 ka based on 10Be ages. Quat. Res. 85, 107–117.
Hughes, P.D., Glasser, N.F., Fink, D., 2022a. 10Be and 26Al exposure history of the highest mountains in Wales: evidence from Yr Wyddfa (Snowdon) and Y Glyderau for a nunatak landscape at the global Last Glacial Maximum. Quat. Sci. Rev. 286, 107523.
Hughes, P.D., Palacios, D., García-Ruiz, J.M., Andrés, N., 2022b. The European glacial landscapes from the Last Glacial Maximum-synthesis. In: European Glacial Landscapes. Elsevier, pp. 507–516.
Huybers, P., 2006. Early Pleistocene glacial cycles and the integrated summer insolation forcing. Science 313, 508–511.
Huybers, P., 2007. Glacial variability over the last two million years: an extended depth-derived agemodel, continuous obliquity pacing, and the Pleistocene progression. Quat. Sci. Rev. 26, 37–55.
Huybers, P., Denton, G., 2008. Antarctic temperature at orbital timescales controlled by local summer duration. Nat. Geosci. 1, 787–792.
Irion, G., Zöllmer, V., 1999. Clay mineral associations in fine-grained surface sediments of the North Sea. J. Sea Res. 41, 119–128.
Jacobsen, S.B., Wasserburg, G., 1980. Sm-Nd isotopic evolution of chondrites. Earth Planet. Sci. Lett. 50, 139–155.
Kisch, H., 1991. Illite crystallinity: recommendations on sample preparation, X-ray diffraction settings, and interlaboratory samples. J. Metamorph. Geol. 9, 665–670.
Kleman, J., Fastook, J., Ebert, K., Nilsson, J., Caballero, R., 2013. Pre-LGM Northern Hemisphere ice sheet topography. Clim. Past 9, 2365–2378.
Koltai, G., Spötl, C., Shen, C., Wu, C., Rao, Z., Palcsu, L., Kele, S., Surányi, G., Bárány-Kevei, I., 2017. A penultimate glacial climate record from southern Hungary. J. Quat. Sci. 32, 946–956.
Krzyszkowski, D., Gizler, H., Jodłowski, J., Dobosz, T., 1999. Quaternary geology and geomorphology in the zone of the maximum extent of the Weichselian icesheet between Sława Śląska and Święciechowa, western Poland. Quatern. Stud. Pol. 16, 47–66.
Kubler, B., 1967. La cristallinité de l'illite et les zones tout à fait supérieures du métamorphisme. Etages tectoniques 105–121.
Kübler, B., Jaboyedoff, M., 2000. Illite crystallinity. Comptes Rendus de l'Académie des Sciences-Series IIA-Earth Planet. Sci. 331, 75–89.

Laban, C., van der Meer, J.J., 2011. Pleistocene glaciation in the Netherlands. In: Developments in Quaternary Sciences. Elsevier, pp. 247–260.
Labeyrie, L., Turon, J.L., Lancelot, Y., 1995. IMAGES 1-MD101 Cruise, RV Marion Dufresne. https://doi.org/10.17600/95200110.
Lambeck, K., Purcell, A., Zhao, J., Svensson, N., 2010. The Scandinavian ice sheet: from MIS 4 to the end of the last glacial maximum. Boreas 39, 410–435.
Laskar, J., Robutel, P., Joutel, F., Gastineau, M., Correia, A., Levrard, B., 2004. A long-term numerical solution for the insolation quantities of the Earth. Astron. Astrophys. 428, 261–285.
Lekens, W.A.H., Haflidason, H., Sejrup, H.P., Nygard, A., Richter, T., Vogt, C., Frederichs, T., 2009. Sedimentation history of the northern North Sea Margin during the last 150 ka. Quat. Sci. Rev. 28, 469–483.
Lüthgens, C., Böse, M., 2011. Chronology of Weichselian main ice marginal positions in north-eastern Germany. E&G Quat. Sci. J. 60, 236–247.
Mangerud, J., 2004. Ice sheet limits on Norway and the Norwegian continental shelf. In: Quaternary Glaciations—Extent and Chronology, 1, pp. 271–294.
Mangerud, J., Bondevik, S., Gulliksen, S., Hufthammer, A.K., Høisæter, T., 2006. Marine 14C reservoir ages for 19th century whales and molluscs from the North Atlantic. Quat. Sci. Rev. 25, 3228–3245.
Marcott, S.A., Clark, P.U., Padman, L., Klinkhammer, G.P., Springer, S.R., Liu, Z., Otto-Bliesner, B.L., Carlson, A.E., Ungerer, A., Padman, J., 2011. Ice-shelf collapse from subsurface warming as a trigger for Heinrich events. Proc. Natl. Acad. Sci. 108, 13415–13419.
Marcott, S.A., Bauska, T.K., Buizert, C., Steig, E.J., Rosen, J.L., Cuffey, K.M., Fudge, T., Severinghaus, J.P., Ahn, J., Kalk, M.L., 2014. Centennial-scale changes in the global carbon cycle during the last deglaciation. Nature 514, 616–619.
Marks, L., Bitinas, A., Błaszkiewicz, M., Börner, A., Guobyte, R., Rinterknecht, V., Tylmann, K., 2022. Northern Central Europe: glacial landforms from the Last Glacial Maximum. In: European Glacial Landscapes. Elsevier, pp. 381–388.
Max, L., Nürnberg, D., Chiessi, C.M., Lenz, M.M., Mulitza, S., 2022. Subsurface ocean warming preceded Heinrich events. Nat. Commun. 13, 4217.
McManus, J.F., Bond, G.C., Broecker, W.S., Johnsen, S., Labeyrie, L., Higgins, S., 1994. High-resolution climate records from the North Atlantic during the last interglacial. Nature 371, 326–329.
Meere, P., 1995. Sub-greenschist facies metamorphism from the Variscides of SW Ireland an early syn-extensional peak thermal event. J. Geol. Soc. 152, 511–521.
Ménot, G., Bard, E., Rostek, F., Weijers, J.W., Hopmans, E.C., Schouten, S., Sinninghe Damsté, J.S., 2006. Early reactivation of European rivers during the last deglaciation. Science 313, 1623–1625.
Merriman, R., Roberts, B., Peacor, D.R., Hirons, S., 1995. Strain-related differences in the crystal growth of white mica and chlorite: a TEM and XRD study of the development of metapelitic microfabrics in the Southern Uplands thrust terrane, Scotland. J. Metamorph. Geol. 13, 559–576.
Mojtahid, M., Eynaud, F., Zaragosi, S., Scourse, J., Bourillet, J.-F., Garlan, T., 2005. Palaeoclimatology and palaeohydrography of the glacial stages on Celtic and Armorican margins over the last 360 000 yrs. Mar. Geol. 224, 57–82.
Monge-Soares, A.M., 1993. The 14 C content of marine shells: evidence for variability in coastal upwelling off Portugal during the Holocene. In: Isotope Techniques in the Study of Past and Current Environmental Changes in the Hydrosphere and the Atmosphere, pp. 471–485.
Moore, D.M., Reynolds, R.C., 1989. X-ray Diffraction and the Identification and Analysis of Clay Minerals. Oxford University Press (OUP).
Moreno, A., Stoll, H., Jiménez-Sánchez, M., Cacho, I., Valero-Garcés, B., Ito, E., Edwards, R.L., 2010. A speleothem record of glacial (25–11.6 kyr BP) rapid climatic changes from northern Iberian Peninsula. Glob. Planet. Chang. 71, 218–231.
Naafs, B.D.A., Hefter, J., Gruetzner, J., Stein, R., 2013. Warming of surface waters in the mid-latitude North Atlantic during Heinrich events. Paleoceanography 28, 153–163.
O'Cofaigh, C., Evans, D.J., 2007. Radiocarbon constraints on the age of the maximum advance of the British–Irish Ice Sheet in the Celtic Sea. Quat. Sci. Rev. 26, 1197–1203.
O'Cofaigh, C., Weilbach, K., Lloyd, J.M., Benetti, S., Callard, S.L., Purcell, C., Chiverrell, R.C., Dunlop, P., Saher, M., Livingstone, S.J., 2019. Early deglaciation of the British-Irish Ice Sheet on the Atlantic shelf northwest of Ireland driven by glacioisostatic depression and high relative sea level. Quat. Sci. Rev. 208, 76–96.
Palacios, D., Stokes, C.R., Phillips, F.M., Clague, J.J., Alcalá-Reygosa, J., Andrés, N., Angel, I., Blard, P.-H., Briner, J.P., Hall, B.L., 2020. The deglaciation of the Americas during the last glacial termination. Earth Sci. Rev. 203, 103113.
Parra, M., Trouky, H., Jouanneau, J.-M., Grousset, F., Latouche, C., Castaing, P., 1998. Étude isotopique (Sr-Nd) de l'origine des dépôts fins holocènes du littoral atlantique (SO France). Oceanol. Acta 21, 631–644.
Patton, H., Hubbard, A., Andreassen, K., Auriac, A., Whitehouse, P.L., Stroeven, A.P., Shackleton, C., Winsborrow, M., Heyman, J., Hall, A.M., 2017. Deglaciation of the Eurasian ice sheet complex. Quat. Sci. Rev. 169, 148–172.
Patton, H., Hubbard, A., Heyman, J., Alexandropoulou, N., Lasabuda, A.P.E., Stroeven, A.P., Hall, A.M., Winsborrow, M., Sugden, D.E., Kleman, J., Andreassen, K., 2022. The extreme yet transient nature of glacial erosion. Nat. Commun. 13.
Peck, V.L., Hall, I.R., Zahn, R., Elderfield, H., Grousset, F., Hemming, S.R., Scourse, J.D., 2006. High resolution evidence for linkages between NW European ice sheet instability and Atlantic Meridional overturning circulation. Earth Planet. Sci. Lett. 243, 476–488.
Pedersen, S.A.S., 2005. Structural analysis of the Rubjerg Knude glaciotectonic complex, Vendsyssel, northern Denmark. GEUS Bull. 8, 1–192.
Penaud, A., Eynaud, F., Turon, J., Zaragosi, S., Malaizé, B., Toucanne, S., Bourillet, J.-F., 2009. What forced the collapse of European ice sheets during the last two glacial periods (150 ka BP and 18 ka cal BP)? Palynological evidence. Palaeogeogr. Palaeoclimatol. Palaeoecol. 281, 66–78.
Peters, K.E., Peters, K.E., Walters, C.C., Moldowan, J., 2005. The Biomarker Guide. Cambridge university press.
Petit, J.-R., Jouzel, J., Raynaud, D., Barkov, N.I., Barnola, J.-M., Basile, I., Bender, M., Chappellaz, J., Davis, M., Delaygue, G., 1999. Climate and atmospheric history of the past 420,000 years from the Vostok ice core, Antarctica. Nature 399, 429.
Primmer, T., 1985. A transition from diagenesis to greenschist facies within a major Variscan fold/thrust complex in SW England. Mineral. Mag. 49, 365–374.
Rasmussen, S.O., Bigler, M., Blockley, S.P., Blunier, T., Buchardt, S.L., Clausen, H.B., Cvijanovic, I., Dahl-Jensen, D., Johnsen, S.J., Fischer, H., 2014. A stratigraphic framework for abrupt climatic changes during the Last Glacial period based on three synchronized Greenland ice-core records: refining and extending the INTIMATE event stratigraphy. Quat. Sci. Rev. 106, 14–28.
Reimer, P.J., Reimer, R.W., 2001. A marine reservoir correction database and on-line interface. Radiocarbon 43, 461–463.
Robinson, D., Bevins, R., 1986. Incipient metamorphism in the Lower Palaeozoic marginal basin of Wales. J. Metamorph. Geol. 4, 101–103.
Roche, D.M., Wiersma, A.P., Renssen, H., 2010. A systematic study of the impact of freshwater pulses with respect to different geographical locations. Clim. Dyn. 34, 997–1013.
Rodrigues, T., Grimalt, J.O., Abrantes, F.G., Flores, J.A., Lebreiro, S.M., 2009. Holocene interdependences of changes in sea surface temperature, productivity, and fluvial inputs in the Iberian continental shelf (Tagus mud patch). Geochem. Geophys. Geosyst. 10.
Rodríguez-Rodríguez, L., Jiménez-Sánchez, M., Domínguez-Cuesta, M.J., Rinterknecht, V., Pallas, R., Bourles, D., 2016. Chronology of glaciations in the Cantabrian Mountains (NW Iberia) during the Last Glacial Cycle based on in situ-produced 10Be. Quat. Sci. Rev. 138, 31–48.
Rolfe, C., Hughes, P., Fenton, C., Schnabel, C., Xu, S., Brown, A., 2012. Paired 26Al and 10Be exposure ages from Lundy: new evidence for the extent and timing of Devensian glaciation in the southern British Isles. Quat. Sci. Rev. 43, 61–73.
Rousseau, D.-D., Zöller, L., Valet, J.-P., 1998. Late Pleistocene climatic variations at Achenheim, France, based on a magnetic susceptibility and Tl chronology of loess. Quat. Res. 49, 255–263.
Salonen, V., Kaakinen, A., Kultti, S., Miettinen, A., Eskola, K.O., Lunkka, J.P., 2008. Middle Weichselian glacial event in the central part of the Scandinavian Ice Sheet recorded in the Hitura pit, Ostrobothnia, Finland. Boreas 37, 38–54.
Sánchez Goñi, M.F.S., Harrison, S.P., 2010. Millennial-scale climate variability and vegetation changes during the Last Glacial: concepts and terminology. Quat. Sci. Rev. 29, 2823–2827.
Sánchez Goñi, M.F., Landais, A., Fletcher, W.J., Naughton, F., Desprat, S., Duprat, J., 2008. Contrasting impacts of Dansgaard–Oeschger events over a western European latitudinal transect modulated by orbital parameters. Quat. Sci. Rev. 27, 1136–1151.
Sánchez Goñi, M.F., Bard, E., Landais, A., Rossignol, L., d'Errico, F., 2013. Air–sea temperature decoupling in western Europe during the last interglacial–glacial transition. Nat. Geosci. 6, 837–841.
Sanchi, L., Ménot, G., Bard, E., 2013. An automated purification method for archaeal and bacterial tetraethers in soils and sediments. Org. Geochem. 54, 83–90.
Schaefer, J.M., Putnam, A.E., Denton, G.H., Kaplan, M.R., Birkel, S., Doughty, A.M., Kelley, S., Barrell, D.J., Finkel, R.C., Winckler, G., 2015. The southern glacial maximum 65,000 years ago and its unfinished termination. Quat. Sci. Rev. 114, 52–60.
Schneider, R., Schmitt, J., Köhler, P., Joos, F., Fischer, H., 2013. A reconstruction of atmospheric carbon dioxide and its stable carbon isotopic composition from the penultimate glacial maximum to the last glacial inception. Clim. Past 9, 2507–2523.
Schouten, S., Hopmans, E.C., Baas, M., Boumann, H., Standfest, S., Könneke, M., Stahl, D. A., Sinninghe Damsté, J.S., 2008. Intact membrane lipids of "Candidatus Nitrosopumilus maritimus," a cultivated representative of the cosmopolitan mesophilic group I crenarchaeota. Appl. Environ. Microbiol. 74, 2433–2440.
Schouten, S., Hopmans, E.C., Sinninghe Damsté, J.S., 2013. The organic geochemistry of glycerol dialkyl glycerol tetraether lipids: a review. Org. Geochem. 54, 19–61.
Scourse, J.D., Hall, I.R., McCave, I.N., Young, J.R., Sugdon, C., 2000. The origin of Heinrich layers: evidence from H2 for European precursor events. Earth Planet. Sci. Lett. 182, 187–195.
Seguinot, J., Ivy-Ochs, S., Jouvet, G., Huss, M., Funk, M., Preusser, F., 2018. Modelling last glacial cycle ice dynamics in the Alps. Cryosphere 12, 3265–3285.
Seierstad, I.K., Abbott, P.M., Bigler, M., Blunier, T., Bourne, A.J., Brook, E., Buchardt, S. L., Buizert, C., Clausen, H.B., Cook, E., 2014. Consistently dated records from the Greenland GRIP, GISP2 and NGRIP ice cores for the past 104 ka reveal regional millennial-scale δ18O gradients with possible Heinrich event imprint. Quat. Sci. Rev. 106, 29–46.
Sejrup, H.P., Hjelstuen, B.O., 2022. The North Sea and Mid-Norwegian continental margin. In: European Glacial Landscapes. Elsevier, pp. 65–73.
Sejrup, H.P., Haflidason, H., Aarseth, I., King, E., Forsberg, C.F., Long, D., Rokoengen, K., 1994. Late Weichselian glaciation history of the northern North Sea. Boreas 23, 1–13.
Sejrup, H., Larsen, E., Landvik, J., King, E., Haflidason, H., Nesje, A., 2000. Quaternary glaciations in southern Fennoscandia: evidence from southwestern Norway and the northern North Sea region. Quat. Sci. Rev. 19, 667–685.
Sejrup, H.P., Hjelstuen, B.O., Dahlgren, K.T., Haflidason, H., Kuijpers, A., Nygård, A., Praeg, D., Stoker, M.S., Vorren, T.O., 2005. Pleistocene glacial history of the NW European continental margin. Mar. Pet. Geol. 22, 1111–1129.
Sejrup, H., Nygård, A., Hall, A., Haflidason, H., 2009. Middle and Late Weichselian (Devensian) glaciation history of south-western Norway, North Sea and eastern UK. Quat. Sci. Rev. 28, 370–380.

Sejrup, H.P., Clark, C.D., Hjelstuen, B.O., 2016. Rapid ice sheet retreat triggered by ice stream debuttressing: evidence from the North Sea. Geology 44, 355–358.
Siegert, M.J., Dowdeswell, J.A., Hald, M., Svendsen, J.-I., 2001. Modelling the Eurasian Ice Sheet through a full (Weichselian) glacial cycle. Glob. Planet. Chang. 31, 367–385.
Sinninghe Damsté, J.S., 2016. Spatial heterogeneity of sources of branched tetraethers in shelf systems: the geochemistry of tetraethers in the Berau River delta (Kalimantan, Indonesia). Geochim. Cosmochim. Acta 186, 13–31.
Sinninghe Damsté, J.S., Schouten, S., Hopmans, E.C., Van Duin, A.C., Geenevasen, J.A., 2002. The characteristic core glycerol dibiphytanyl glycerol tetraether membrane lipid of cosmopolitan pelagic crenarchaeota. J. Lipid Res. 43, 1641–1651.
Southon, J., Noronha, A.L., Cheng, H., Edwards, R.L., Wang, Y., 2012. A high-resolution record of atmospheric 14C based on Hulu Cave speleothem H82. Quat. Sci. Rev. 33, 32–41.
Stone, P., Evans, J., 2000. Silurian provenance variation in the Southern Uplands terrane, Scotland, assessed using neodymium isotopes and linked with regional tectonic evolution. Earth Environ. Sci. Trans. R. Soc. Edinb. 91, 447–455.
Stroeven, A.P., Hättestrand, C., Kleman, J., Heyman, J., Fabel, D., Fredin, O., Goodfellow, B.W., Harbor, J.M., Jansen, J.D., Olsen, L., 2016. Deglaciation of fennoscandia. Quat. Sci. Rev. 147, 91–121.
Stuiver, M., Braziunas, T.F., 1993. Modeling atmospheric 14C influences and 14C ages of marine samples to 10,000 BC. Radiocarbon 35, 137–189.
Stuiver, M., Pearson, G.W., Braziunas, T., 1986. Radiocarbon age calibration of marine samples back to 9000 cal yr BP. Radiocarbon 28, 980–1021.
Svendsen, J.I., Alexanderson, H., Astakhov, V.I., Demidov, I., Dowdeswell, J.A., Funder, S., Gataullin, V., Henriksen, M., Hjort, C., Houmark-Nielsen, M., 2004. Late Quaternary ice sheet history of northern Eurasia. Quat. Sci. Rev. 23, 1229–1271.
Tanaka, T., Togashi, S., Kamioka, H., Amakawa, H., Kagami, H., Hamamoto, T., Dragusanu, C., 2000. JNdi-1: a neodymium isotopic reference in consistency with LaJolla neodymium. Chem. Geol. 168 (3–4), 279–281.
Teale, C.T., Spears, D.A., 1986. The mineralogy and origin of some Silurian bentonites, Welsh Borderland, UK. Sedimentology 33, 757–765.
Tisnérat-Laborde, N., Paterne, M., Métivier, B., Arnold, M., Yiou, P., Blamart, D., Raynaud, S., 2010. Variability of the northeast Atlantic sea surface Δ14C and marine reservoir age and the North Atlantic Oscillation (NAO). Quat. Sci. Rev. 29, 2633–2646.
Toucanne, S., Zaragosi, S., Bourillet, J.-F., Naughton, F., Cremer, M., Eynaud, F., Dennielou, B., 2008. Activity of the turbidite levees of the Celtic–Armorican margin (Bay of Biscay) during the last 30,000 years: imprints of the last European deglaciation and Heinrich events. Mar. Geol. 247, 84–103.
Toucanne, S., Zaragosi, S., Bourillet, J.-F., Cremer, M., Eynaud, F., Van Vliet-Lanoë, B., Pénaud, A., Fontanier, C., Turon, J.L., Cortijo, E., 2009. Timing of massive 'Fleuve Manche'discharges over the last 350 kyr: insights into the European ice-sheet oscillations and the European drainage network from MIS 10 to 2. Quat. Sci. Rev. 28, 1238–1256.
Toucanne, S., Zaragosi, S., Bourillet, J.-F., Marieu, V., Cremer, M., Kageyama, M., Van Vliet-Lanoë, B., Eynaud, F., Turon, J.-L., Gibbard, P.L., 2010. The first estimation of Fleuve Manche palaeoriver discharge during the last deglaciation: evidence for Fennoscandian ice sheet meltwater flow in the English Channel ca 20–18 ka ago. Earth Planet. Sci. Lett. 290, 459–473.
Toucanne, S., Soulet, G., Freslon, N., Jacinto, R.S., Dennielou, B., Zaragosi, S., Eynaud, F., Bourillet, J.-F., Bayon, G., 2015. Millennial-scale fluctuations of the European Ice Sheet at the end of the last glacial, and their potential impact on global climate. Quat. Sci. Rev. 123, 113–133.
Toucanne, S., Soulet, G., Vázquez Riveiros, N., Boswell, S.M., Dennielou, B., Waelbroeck, C., Bayon, G., Mojtahid, M., Bosq, M., Sabine, M., 2021. The North Atlantic Glacial Eastern boundary current as a key driver for ice-sheet—AMOC interactions and climate instability. Paleoceanogr. Paleoclimatol. 36 e2020PA004068.
Turon, J.-L., Bourillet, J.-F., 2004. MD142 / ALIENOR 2 Cruise, RV Marion Dufresne. https://doi.org/10.17600/4200200.
Waelbroeck, C., Labeyrie, L., Michel, E., Duplessy, J.-C., Mcmanus, J.F., Lambeck, K., Balbon, E., Labracherie, M., 2002a. Sea-level and deep water temperature changes derived from benthic foraminifera isotopic records. Quat. Sci. Rev. 21, 295–305.
Waelbroeck, C., Labeyrie, L., Michel, E., Duplessy, J.-C., Mcmanus, J.F., Lambeck, K., Balbon, E., Labracherie, M., 2002b. Sea-level and deep water temperature changes derived from benthic foraminifera isotopic records. Quat. Sci. Rev. 21, 295–305.
WAIS Divide Project Members, 2015. Precise interpolar phasing of abrupt climate change during the last ice age. Nature 520, 661.
Wang, Y.-J., Cheng, H., Edwards, R.L., An, Z., Wu, J., Shen, C.-C., Dorale, J.A., 2001. A high-resolution absolute-dated late Pleistocene monsoon record from Hulu Cave, China. Science 294, 2345–2348.
Wang, Y., Cheng, H., Edwards, R.L., Kong, X., Shao, X., Chen, S., Wu, J., Jiang, X., Wang, X., An, Z., 2008. Millennial-and orbital-scale changes in the East Asian monsoon over the past 224,000 years. Nature 451, 1090–1093.
Warr, L., Primmer, T., Robinson, D., 1991. Variscan very low-grade metamorphism in southwest England: a diastathermal and thrust-related origin. J. Metamorph. Geol. 9, 751–764.
Wary, M., Eynaud, F., Swingedouw, D., Masson-Delmotte, V., Matthiessen, J., Kissel, C., Zumaque, J., Rossignol, L., Jouzel, J., 2017. Regional seesaw between the North Atlantic and Nordic Seas during the last glacial abrupt climate events. Clim. Past 13, 729–739.
Weckwerth, P., 2010. Evolution of the Toruń Basin in the Late Weichselian. Landf. Anal. 14, 57–84.
Weijers, J.W., Schouten, S., Spaargaren, O.C., Sinninghe Damsté, J.S., 2006. Occurrence and distribution of tetraether membrane lipids in soils: implications for the use of the TEX86 proxy and the BIT index. Org. Geochem. 37, 1680–1693.
Weijers, J.W., Schefuß, E., Kim, J.-H., Sinninghe Damsté, J.S., Schouten, S., 2014. Constraints on the sources of branched tetraether membrane lipids in distal marine sediments. Org. Geochem. 72, 14–22.
Wilson, D.J., Bertram, R.A., Needham, E.F., van de Flierdt, T., Welsh, K.J., McKay, R.M., Mazumder, A., Riesselman, C.R., Jimenez-Espejo, F.J., Escutia, C., 2018. Ice loss from the East Antarctic Ice Sheet during late Pleistocene interglacials. Nature 561, 383–386.
Woerther, P., 2013. VT133 / MERIADZEC Cruise, RV Marion Dufresne. https://doi.org/10.17600/13200040.
Woillard, G.M., 1978. Grande Pile peat bog: a continuous pollen record for the last 140,000 years. Quat. Res. 9, 1–21.
Wu, W., Zhao, L., Pei, Y., Ding, W., Yang, H., Xu, Y., 2013. Variability of tetraether lipids in Yellow River-dominated continental margin during the past eight decades: implications for organic matter sources and river channel shifts. Org. Geochem. 60, 33–39.
Xiao, W., Wang, Y., Zhou, S., Hu, L., Yang, H., Xu, Y., 2016. Ubiquitous production of branched glycerol dialkyl glycerol tetraethers (brGDGTs) in global marine environments: a new source indicator for brGDGTs. Biogeosciences 13, 5883–5894.
Zaragosi, S., Eynaud, F., Pujol, C., Auffret, G.A., Turon, J.-L., Garlan, T., 2001. Initiation of the European deglaciation as recorded in the northwestern Bay of Biscay slope environments (Meriadzek Terrace and Trevelyan Escarpment): a multi-proxy approach. Earth Planet. Sci. Lett. 188, 493–507.
Zaragosi, S., Bourillet, J.-F., Eynaud, F., Toucanne, S., Denhard, B., Van Toer, A., Lanfumey, V., 2006. The impact of the last European deglaciation on the deep-sea turbidite systems of the Celtic-Armorican margin (Bay of Biscay). Geo-Mar. Lett. 26, 317–329.
Zell, C., Kim, J.-H., Moreira-Turcq, P., Abril, G., Hopmans, E.C., Bonnet, M.-P., Sobrinho, R.L., Sinninghe Damsté, J.S., 2013. Disentangling the origins of branched tetraether lipids and crenarchaeol in the lower Amazon River: implications for GDGT-based proxies. Limnol. Oceanogr. 58, 343–353.
Zell, C., Kim, J.-H., Dorhout, D., Baas, M., Sinninghe Damsté, J.S., 2015. Sources and distributions of branched tetraether lipids and crenarchaeol along the Portuguese continental margin: implications for the BIT index. Cont. Shelf Res. 96, 34–44.
Zhou, Y., McManus, J.F., Jacobel, A.W., Costa, K.M., Wang, S., Caraveo, B.A., 2021. Enhanced iceberg discharge in the western North Atlantic during all Heinrich events of the last glaciation. Earth Planet. Sci. Lett. 564, 116910.
Zumaque, J., Eynaud, F., de Vernal, A., 2017. Holocene paleoceanography of the Bay of Biscay: evidence for West-East linkages in the North Atlantic based on dinocyst data. Palaeogeogr. Palaeoclimatol. Palaeoecol. 468, 403–413.